

# Volatile Organic Compound Detection Using Insect Odorant-Receptor Functionalised Field-Effect Transistors

by

Eddyn Oswald Perkins Treacher

A thesis submitted in fulfilment of the  
requirements of the degree of  
Doctor of Philosophy in Physics  
School of Physical and Chemical Sciences  
Te Herenga Waka - Victoria University of Wellington

Mar 2024





# Table of contents

<b>Acknowledgements</b>	<b>1</b>
<b>1. Characteristics of Pristine Carbon Nanotube &amp; Graphene Field Effect Transistors</b>	<b>3</b>
1.1. Introduction . . . . .	3
1.2. Carbon Nanotube Network Morphology and Composition . . . . .	4
1.2.1. Atomic Force Microscopy . . . . .	4
1.2.2. Raman Spectroscopy . . . . .	10
1.3. Electrical Characteristics of Pristine Devices . . . . .	12
1.3.1. Python Analysis . . . . .	12
1.3.2. Carbon Nanotube Network Devices . . . . .	14
1.3.3. Graphene Devices . . . . .	19
1.4. Aqueous Sensing of Phosphate Buffered Saline Concentration . . . . .	21
1.4.1. Control Series and Baseline Drift . . . . .	21
1.4.2. Sensing Series . . . . .	25
1.5. Vapour Sensing with Ethyl Hexanoate . . . . .	30
1.5.1. Baseline Drift . . . . .	30
1.5.2. Sensing Series . . . . .	33
1.6. Conclusion . . . . .	36
<b>Appendices</b>	<b>39</b>
<b>A. Vapour System Hardware</b>	<b>39</b>
<b>B. Python Code for Data Analysis</b>	<b>41</b>
B.1. Code Repository . . . . .	41
B.2. Atomic Force Microscope Histogram Analysis . . . . .	41
B.3. Raman Spectroscopy Analysis . . . . .	41
B.4. Field-Effect Transistor Analysis . . . . .	41



# Acknowledgements

69450

Rifat, Alex - vapour sensor  
Erica Cassie - FET sensing setup  
Rob Keyzers and Jennie Ramirez-Garcia - NMR spectra  
Patricia Hunt - Computational chemistry



# 1. Characteristics of Pristine Carbon Nanotube & Graphene Field Effect Transistors

## 1.1. Introduction

A range of methods were followed to fabricate carbon nanotube network and graphene field-effect transistors for biosensor use. This chapter therefore looks to use the characterisation techniques outlined in the previous chapter to compare and contrast the device channel morphologies and electrical characteristics resulting from various methods.

The three carbon nanotube film types used for devices were the solvent-deposited, surfactant-deposited and steam-assisted surfactant-deposited (steam-deposited) films discussed in the previous chapter. As minor changes were made to fabrication processes throughout the thesis, the fabrication dates of devices used are stated, which can be cross-referenced with **?@sec-fabrication** to identify the specific process used. Atomic force microscopy and Raman spectroscopy was performed on the carbon nanotube networks to identify the distribution of carbon nanotube diameters and the defects present on the carbon nanotube networks. Electrical characterisation was then used to see how the morphology of each film type affects the performance of the completed devices. Both back-gated and liquid-gated transfer characteristics were compared, as well as key parameters taken from the liquid-gated characteristics. The electrical behaviour of liquid-gated graphene devices was also examined, as well as the impact of water on the performance of back-gated devices for vapour sensing use.

Finally, as a control measurement for liquid-gated sensing and to verify the behaviour of the pristine device as a sensor, a salt concentration sensing series was performed with a steam-deposited carbon nanotube network device. The device characteristics were taken and device drift was examined and modelled. The sensing series was performed by successively diluting 1XPBS electrolyte in the polydimethylsiloxane ‘well’ (electrolyte container) while passing a current through the device, and measuring the current response to dilutions. Various filters were applied to the collected data to better understand the signal change.

## 1.2. Carbon Nanotube Network Morphology and Composition

### 1.2.1. Atomic Force Microscopy

Figure 1.1 shows a side-by-side comparison of the surface morphology of carbon nanotube films fabricated using the methods described in ?@sec-dep-carbon-nanotubes. These images were collected using an atomic force microscope and processed in the manner described in ?@sec-afm-characterisation. Figure 1.1a shows a film of carbon nanotubes deposited in solvent, Figure 1.1c shows a film of carbon nanotubes dropcast in surfactant, and Figure 1.1e shows carbon nanotubes dropcast in surfactant in the presence of steam. As discussed in previous works using solvent-based deposition techniques for depositing carbon nanotubes, in each network multi-tube bundles form due to strong mutual attraction between nanotubes [1]–[4]. However, when surfactants are present, they adsorb onto the carbon nanotubes and form a highly repulsive structure able to overcome the strong attraction between nanotubes. This repulsion keeps the individual carbon nanotubes more isolated [5]–[9]. The diameter range provided by the supplier for the individual carbon nanotubes used is 1.2 – 1.7 nm, while the length range is 0.3 – 5.0  $\mu\text{m}$  (Nanointegris).

It has previously been demonstrated that the diameter range of deposited single-walled carbon nanotubes can be modelled via a normal or Gaussian distribution [10]–[12]. However, when the height profiles from the  $2.5 \mu\text{m} \times 2.5 \mu\text{m}$  AFM images are directly extracted and binned, as plotted in black in Figure 1.1, the histograms obtained do not follow a normal distribution. One reason for this result is the surface roughness of the silicon dioxide substrate. The carbon nanotubes do not lie perfectly level on a perfectly level silicon oxide substrate. In practice, both the  $\text{SiO}_2$  substrate and the surface of the carbon nanotubes both have a degree of roughness. To find the contribution of surface roughness to the height profile histogram corresponding to each network deposition method, silicon dioxide substrates were modified using the same processes as in Figure 1.1 but without carbon nanotubes present in the solutions used.  $2.5 \mu\text{m} \times 2.5 \mu\text{m}$  AFM images of the modified surfaces are shown in Figure 1.2.

In Figure 1.2, it appears that each substrate surface has a roughness that follows a normal distribution with some degree of skewness. Figure 1.2b and Figure 1.2d are negatively skewed distributions. The fitted skew-normal distribution in Figure 1.2b has a skew parameter  $\alpha$  (or shape parameter) of -3.2, a location parameter  $\xi$  of 2.2 nm and a scale parameter  $\omega$  of 0.5 nm, while in Figure 1.2d  $\alpha = -2.2$ ,  $\xi = 2.2$  nm and  $\omega = 0.5$  nm.  $\xi$  and  $\omega$  correspond to the mean and standard deviation of the skew-free normal distribution when  $\alpha$  is set equal to zero [13]. The close correspondence between  $\xi$  and  $\omega$  for these distributions but not  $\alpha$  implies that the skewness is a variable imaging or processing artifact rather than a physical property of the surface. Without distortion, the roughness of a clean  $\text{SiO}_2$  surface should follow a normal distribution [14].

## 1.2. Carbon Nanotube Network Morphology and Composition

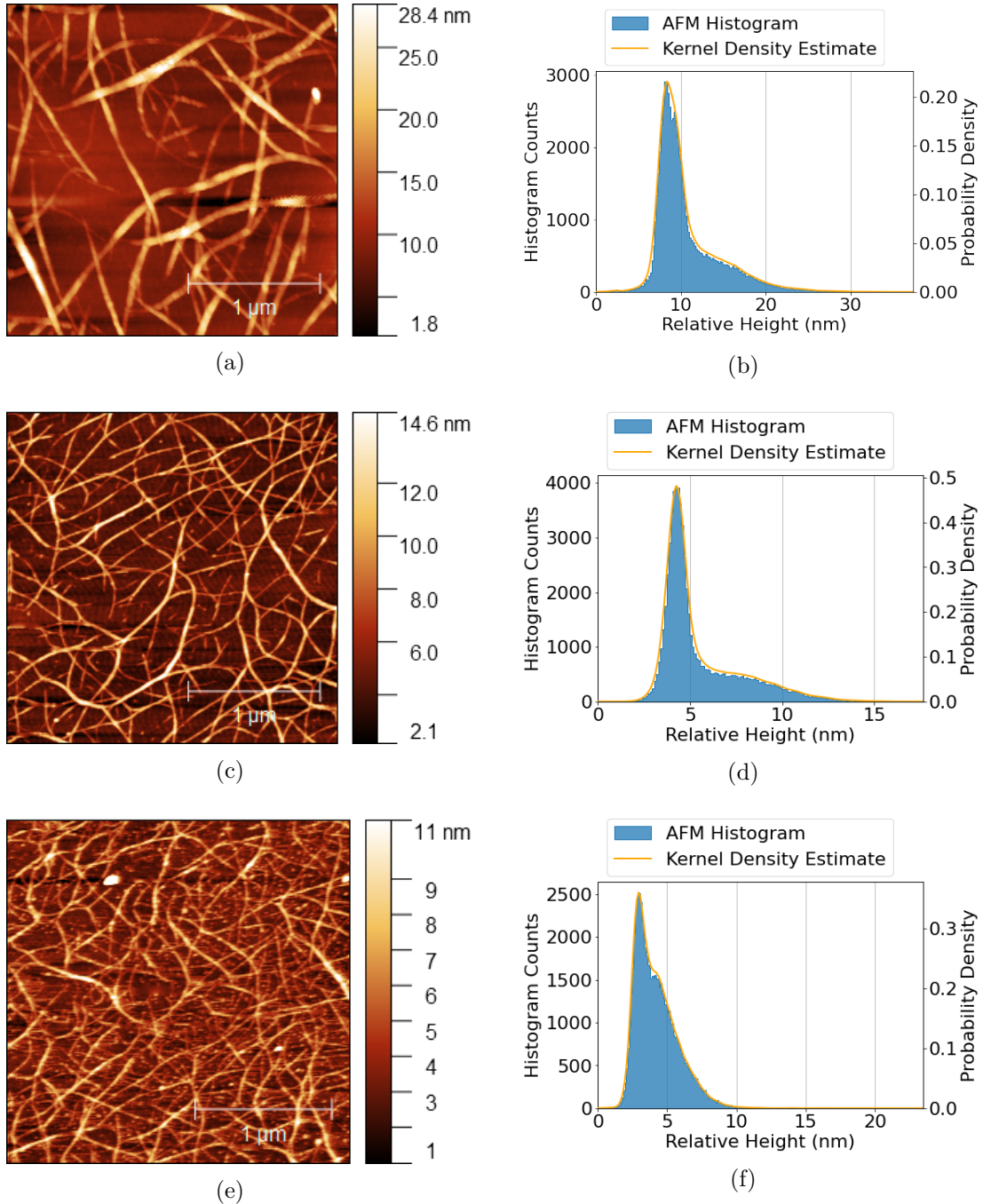


Figure 1.1.:  $2.5 \mu\text{m} \times 2.5 \mu\text{m}$  atomic force microscope (AFM) images of carbon nanotube films deposited using various methods, shown side-by-side with histogram height distributions and kernel density estimate (KDE) plots corresponding to each image. The network shown in (a) with height distribution shown in (b) was deposited in solvent, the network shown in (c) with height distribution shown in (d) was dropcast in surfactant, and the network shown in (e) with height distribution shown in (f) was dropcast in surfactant with steam present.

## 1. Characteristics of Pristine Carbon Nanotube & Graphene Field Effect Transistors

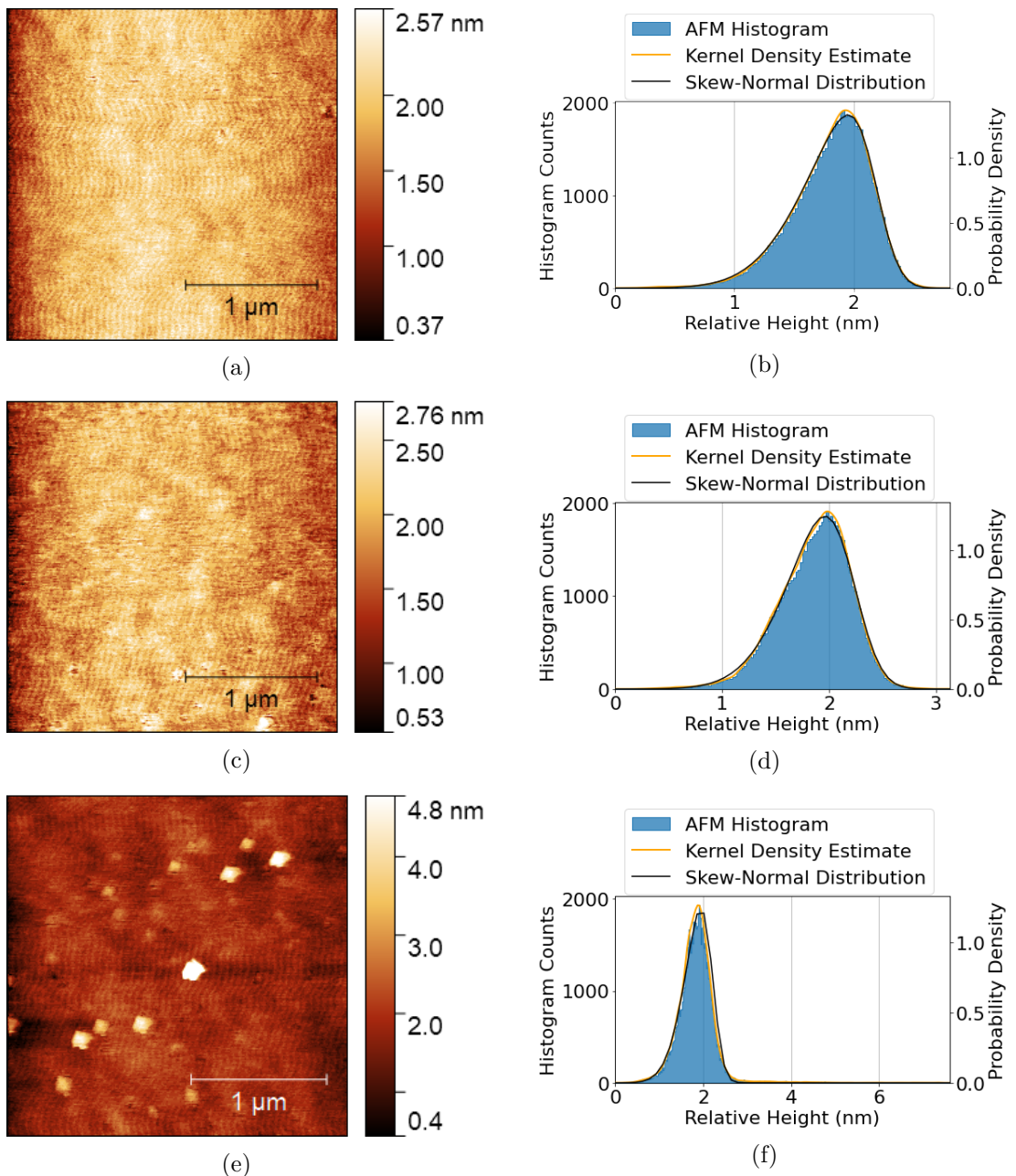


Figure 1.2.:  $2.5 \mu\text{m} \times 2.5 \mu\text{m}$  atomic force microscope (AFM) images of silicon dioxide substrates alongside histogram height distributions and KDE plots corresponding to each image. The substrate in (a) and (b) was exposed to solvent, the substrate in (c) and (d) was exposed to surfactant, and the substrate in (e) and (f) was exposed to surfactant with steam present.

## 1.2. Carbon Nanotube Network Morphology and Composition

However, Figure 1.2f has a pronounced positive skew with a long tail. The tail appears to result from the contribution of residual surfactant aggregates to surface morphology, observed in Figure 1.2e and recently discussed elsewhere in the literature [12], [15]. Attempting to fit a skew-normal distribution to this histogram fails when all three variables are allowed to vary due to the presence of the tail. Instead, previous values obtained for  $\xi$  and  $\omega$  can be used for the fitting process, with only  $\alpha$  allowed to change. Fixing  $\xi$  and  $\omega$  at 2.2 nm and 0.5 nm respectively gives the result shown in Figure 1.2f. The fitted distribution has an  $\alpha$  of -2.4. The distribution closely fits the negative tail of the histogram, but deviates slightly from the positive tail due to the presence of surfactant. Since this deviation is small, the quality of the fit is still reasonably high, with an R-squared value of 0.98. Surfactant contamination could have negative effects on both sensitivity of carbon nanotubes and also could damage attached biological elements.

Using the morphology analysis technique outlined by Vobornik *et al.* [12], five successive diameter measurements of 30 carbon nanotube bundles were collected using Gwyddion. Measurements were not taken at bundle junctions. A height threshold ‘mask’ was defined in Gwyddion to determine average substrate height, as shown in Figure 1.3a. This background value was subtracted from our diameter measurements to determine the actual bundle height. The means of the solvent-deposited, surfactant-deposited and steam-assisted surfactant-deposited bundle diameter histograms are  $8.8 \pm 4.0$  nm,  $4.2 \pm 1.8$  nm and  $3.3 \pm 1.0$  nm respectively. An increased maximum feature height leads to an increased mean background height, and by examining the AFM images in Figure 1.1 it appears this may be due to deep artifacts on the surface of the substrate in the vicinity of large features. The average of the five height-adjusted values for each carbon nanotube bundle was then calculated, and these 30 averages were sorted into six equal-sized bins. The binned bundle diameter measurements, alongside estimated probability density, are shown in Figure 1.3.

From Figure 1.3, it is clear that each histogram appears to follow a positively skewed normal distribution, different to the skew-free normal distribution expected from previous works [10]–[12]. The skew is likely another artifact from imaging the network with the atomic force microscope. The force of the atomic force microscope tip is known to cause larger bundles to undergo some degree of compression, and the resulting systematic underestimation of their height may be responsible for the distribution skewness [12]. The fitted skew-normal distribution in Figure 1.3b has  $\alpha = 2.7$ ,  $\xi = 4.3$  nm,  $\omega = 5.9$  nm, the distribution in Figure 1.3c has  $\alpha = 2.4$ ,  $\xi = 2.2$  nm,  $\omega = 2.6$  nm, and the distribution in Figure 1.3d has  $\alpha = 3.6$ ,  $\xi = 2.2$  nm and  $\omega = 1.5$  nm. The probability density for the carbon nanotube bundle histogram drops to approximately zero at or before 0 nm, which is physically appropriate.

Warning: package 'kableExtra' was built under R version 4.3.3

1. Characteristics of Pristine Carbon Nanotube & Graphene Field Effect Transistors

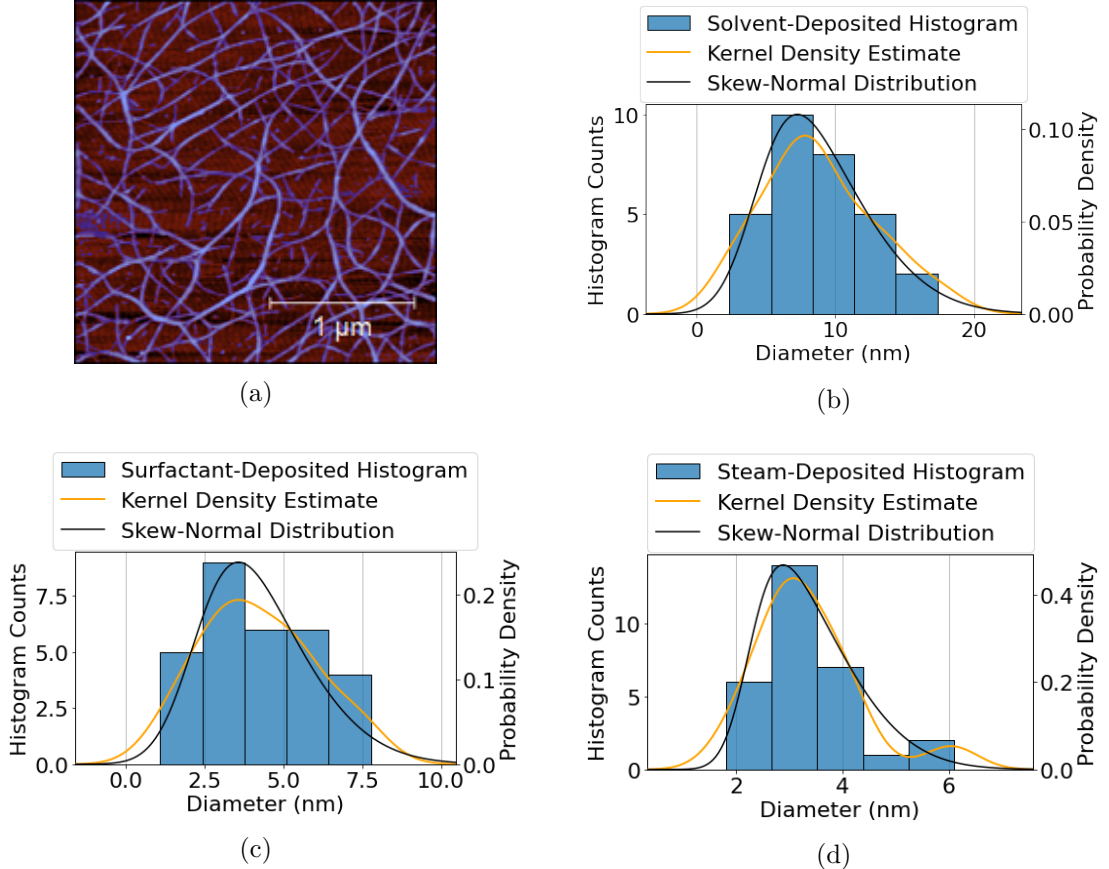


Figure 1.3.: An masked AFM image is shown in (a), where the masked carbon nanotube bundles are shaded blue. The mask sets a height threshold so that masked features are excluded from the height dataset. Histogram height distributions with corresponding KDE plots collected via the morphology analysis method outlined by Vobornik *et al.* [12] are shown in (b)-(d). The substrate in (b) was exposed to solvent, the substrate in (c) was exposed to surfactant, and the substrate in (d) was exposed to surfactant with steam present.

## 1.2. Carbon Nanotube Network Morphology and Composition

Table 1.1.: The first eight optimised ratios of 2D packed circle diameter to encompassing circle diameter, given to 3 s.f. (encompassing circle diameter =  $d$ , number of packed circles =  $n$ , approximate packed circle diameter =  $d_n$ ).

$n$	2	3	4	5	6	7	8	9
$d/d_n$	2.00	2.15	2.41	2.70	3.00	3.00	3.30	3.61

Previously, analysis of the morphology of carbon nanotube networks has been simplified by assuming the component nanotubes are cylinders, follow 2D packing and are of equal diameter [2]. Table 1.1 shows the relationship between the diameter of a bundle of 2D packed cylinders and the constituent diameters of up to nine cylinders within that bundle. From looking up the relevant  $d/d_n$  packing ratios, and assuming an average carbon nanotube diameter of 1.45 nm, it is possible to use to find the approximate number of nanotubes  $n$  likely to be present in the mean bundle size corresponding to each deposition type [16], [17]. These estimates are shown in Table 1.2. Also shown in Table 1.2 is an estimate of the ratio of single- to multi-tube bundles for each deposition. This estimate was obtained by taking the integral of each distribution with a lower bound of 2.9 nm, the minimum multi-tube bundle size for 1.45 nm diameter nanotubes. As the area under the curve represents the probability a bundle will have a particular diameter, this integral should give a good estimate of the relative proportion of multi-tube bundles. Table 1.2 should be interpreted as lower-limit estimates of the size and relative proportion of bundles, recalling that the distribution skewness indicates underestimation of the true bundle height.

Table 1.2.: The mean of histogram distributions for carbon nanotube films deposited using various methods, alongside estimates for the number of nanotubes present per mean bundle and the estimated proportion of multi-tubed bundles present across the network.

	Mean Bundle Diameter (nm)	Tubes per Average Bundle	% Multi-Tube Bundles
Solvent deposited	$8.8 \pm 4.0$	28	> 96%
Surfactant deposited	$4.2 \pm 1.8$	5	> 75%
Surfactant deposited with steam	$3.3 \pm 1.0$	3	> 65%

Both the carbon nanotube bundle diameter mean and standard deviation are small for surfactant-deposited films when compared to the mean and standard deviation of solvent-deposited films. However, despite the presence of surfactant, it is apparent both from Figure 1.1 and Table 1.2 that not all surfactant-dispersed carbon nanotubes are deposited individually. Bundling may occur during the process of deposition onto the

## *1. Characteristics of Pristine Carbon Nanotube & Graphene Field Effect Transistors*

substrate, which could disrupt the repulsive forces from the surfactant coating and allow attractive forces to temporarily dominate. It is possible that the bundling of surfactant-dispersed carbon nanotubes is a consequence of dynamics introduced by the coffee-ring effect [18], [19]. The coffee-ring effect refers to a build-up of dispersed solid forming around the edges of a dispersion evaporating on a surface. This process occurs due to the dispersion edges being fixed by surface forces, leading to capillary flow outwards to replace liquid evaporating at the edges, bringing solid material along with it. The presence of vapour is known to disrupt this capillary effect [20], which may explain why mean bundle diameter is lower for the films deposited in surfactant with steam present relative to films deposited in surfactant without steam.

The discussion in this section gives us a new understanding of the histograms shown in Figure 1.1. It is now apparent that these histograms are linear combinations of skewed normal distributions. These distributions include a negatively-skewed distribution corresponding to the substrate surface and a positively-skewed distribution corresponding to the carbon nanotube bundles. X and Y junctions between overlapping nanotubes may also form a similarly skewed normal distribution as part of the full histogram [2]. The complete linear combination could be modelled mathematically in order to rapidly extract key parameters from atomic force microscope images [21], but implementing this approach is outside of the scope of this thesis. Another outcome of this discussion is awareness that carbon nanotube bundling within a network is lowered by the presence of surfactant during deposition. Introducing steam when depositing with surfactant lowers bundling even further, but also leads to residual surfactant pooling and attaching to the substrate surface. These results may both be explained by the presence of steam enabling surfactant to follow carbon nanotubes to the substrate surface, which keeps them from bundling during the attachment process. The unwanted persistence of surfactant means that higher temperature vacuum annealing may be required for robust biosensors [22].

### **1.2.2. Raman Spectroscopy**

Raman spectroscopy was also used to analyse and compare the deposited carbon nanotube networks. Raman spectra were collected from a solvent-deposited carbon nanotube film and a steam-assisted surfactant-deposited film, both on silicon dioxide, in the manner described in [?@sec-raman-characterisation](#). These spectra were then processed using the Python script mentioned in Section B.3. For each location, spectra over two wavenumber ranges were collected. A peak corresponding to the silicon dioxide substrate, found in the range between  $100\text{ cm}^{-1}$  and  $650\text{ cm}^{-1}$ , was used as a reference peak for the normalisation of intensity across the wavenumber range between  $1300\text{ cm}^{-1}$  and  $1650\text{ cm}^{-1}$ . These normalised spectra are shown in Figure 1.4. In all spectra, a D-band comprising a single D-peak is observed at  $\sim 1320\text{ cm}^{-1}$ , and a G-band comprising two G-peaks,  $G^-$  and  $G^+$ , is observed between  $\sim 1525\text{ cm}^{-1}$  and  $\sim 1650\text{ cm}^{-1}$ . These features are characteristic of networks of semiconducting carbon nanotubes [23], [24].

## 1.2. Carbon Nanotube Network Morphology and Composition

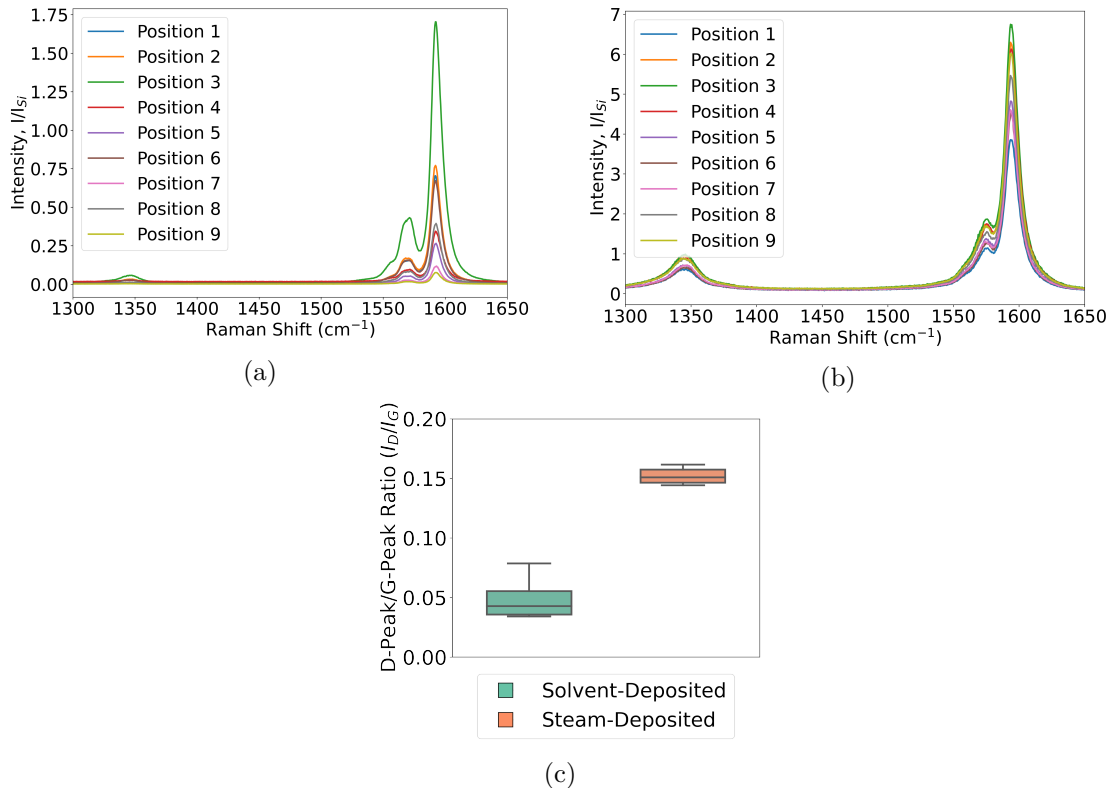


Figure 1.4.: A series of nine Raman spectra at different locations across a  $40 \mu\text{m} \times 100 \mu\text{m}$  carbon nanotube film region, where (a) shows spectra from a film deposited using solvent while (b) shows spectra from a film deposited with surfactant in the presence of steam. (c) shows the spread of the D-peak/G<sup>+</sup>-peak spectral ratios corresponding to each film.

## *1. Characteristics of Pristine Carbon Nanotube & Graphene Field Effect Transistors*

Closer inspection of the D peak and G peaks can give us important information about network composition.  $G^-$  is a minor peak found at  $\sim 1570 \text{ cm}^{-1}$ , while  $G^+$  is a larger feature at  $\sim 1590 \text{ cm}^{-1}$ . The  $G^+$  feature describes the in-plane vibration of carbon bonds along the length of the carbon nanotubes, while the  $G^-$  feature describes the in-plane vibration of bonds about the nanotube circumference [24], [25]. The splitting between the wavenumber location of the  $G^-$  and  $G^+$  local maxima is lower in Figure 1.4b than in Figure 1.4a, indicating more metallic nanotubes are present in the surfactant-deposited network [25]. The D-peak gives an indication of the defects present in the carbon nanotube atomic structure [24], [25]. The size of the normalised D-peak appears much lower in Figure 1.4a than in Figure 1.4b, indicating the solvent deposition process introduces less defects to the carbon nanotubes than surfactant-mediated deposition.

It is also possible to compare the relative magnitude of the D-peak and  $G^+$ -peak intensity to quantify carbon nanotube structural disorder, which disrupts in-plane lattice vibration [23], [24]. Figure 1.4c gives a summary of the ratios between the D-peak and  $G^+$ -peak across all nine positions for the solvent-deposited and surfactant-deposited film. It is immediately observed that  $I_D/I_G$  is significantly larger for the steam-assisted, surfactant-deposited films than for the solvent-deposited films. This is a further indication of the presence of defects across the steam-deposited network. These defects are likely introduced through the introduction of charge impurities by surfactant aggregates present around the carbon nanotubes [15]. However, at the same time, the range of values for the  $I_D/I_G$  ratio is lower for the steam-deposited network. This spatially homogeneous vibrational behaviour implies the steam-deposited network is more evenly distributed than the solvent-deposited network, which matches the discussion in Section 1.2.

## **1.3. Electrical Characteristics of Pristine Devices**

### **1.3.1. Python Analysis**

Analysis of electrical measurements was performed using the three modules described in Section B.4. The first of the three modules is for processing sensing datasets. This module cleans, analyses and filters sensing data and produces a variety of plots. These plots include normalised plots (type of normalisation can be set in the code config file), plots with fitted curves, plots with the linear baseline drift removed, plots of signal with analyte addition, “despiked” plots and “filtered” plots. The analysis used to produce these plots is described further below. It is possible to add annotations to any of these plots using the config file, and it is possible to produce a plot with a combination of these modifications. The module can also fit exponential and linear trendlines to regions of the sensing data, and find the signal change per analyte addition; the module then returns spreadsheets containing the results of these analyses, including the standard deviation for all calculated parameters.

### 1.3. Electrical Characteristics of Pristine Devices

The `scipy.optimize.curve_fit` function is used in the first module to fit linear and exponential curves to regions of interest of the sensing data. For a linear fit  $c_1 t + c_2$ , initial parameters are simply set as  $c_1 = 1$  and  $c_2 = 0$ . For an exponential fit  $I_0 \exp(-t/\tau) + I_C$ , rough approximations are used for the initial parameters:  $I_C$  is set as the final current measurement of the region of interest,  $I_0$  is set as the initial current measurement minus  $I_C$ , and  $\tau$  is set as the time where current has dropped to  $e^{-1}I_0 + I_C$ .

“Despiked” plots have had spurious datapoints removed through the use of an interquartile range rolling filter. The window size of the rolling filter used was 40 datapoints, and datapoints in each window with a z-score above  $\pm 3$  were removed from the plotted/processed data. “Filtered” plots had noise reduced using a moving median filter. The moving median filter is more effective at removing noise than a simple moving average, and has advantages over other filters (such as the Savitzky-Golay filter) when removing noise from data with sharp edges, as is the case for sensing data. Median filtering can also be used for baseline drift compensation, though this approach was not used in this thesis [26]. The moving median filter used had a window of 40 datapoints.

Plots of signal with analyte addition were constructed from current data after first removing baseline drift and applying a moving median filter. A simple difference calculation between the mean of the filtered current before an addition and the mean of the filtered current after the addition was performed at each addition. These differences were then normalised relative to the initial current. The signal with analyte addition give reasonably consistent results regardless of whether baseline drift was removed from the data, as shown in Figure 1.5. We can therefore be confident that robust signal with analyte addition plots are robust even in the presence of significant drift.

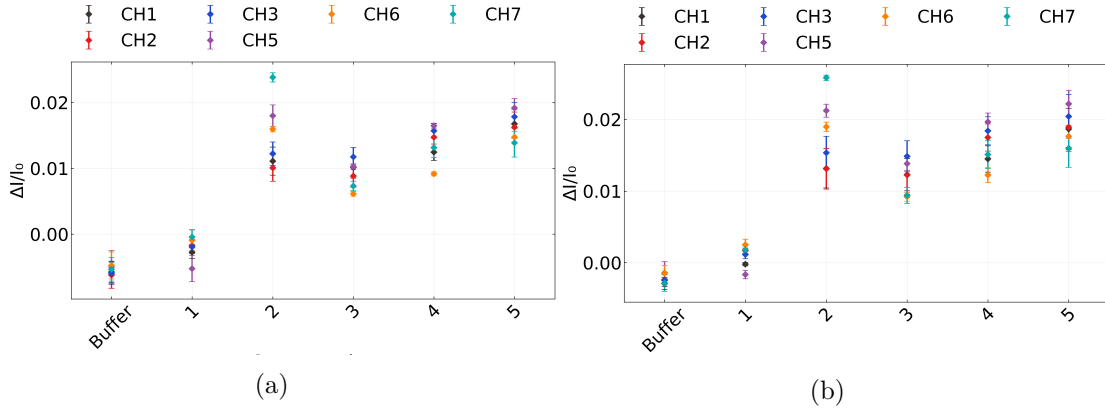


Figure 1.5.: A comparison of signal with analyte addition plots taken from the same salt concentration sensing dataset (the same dataset as used in Figure 1.11). In (a), a simple difference calculation performed on filtered data was used, while in (b) the same calculation was performed on filtered data with the baseline drift removed, the method used in the body of the thesis.

The second module creates combined and individual plots of transfer data collected

## 1. Characteristics of Pristine Carbon Nanotube & Graphene Field Effect Transistors

from eight channels on a single device. In combined plots, channels which are non-working, due to being shorted or non-conducting, are removed via setting a maximum and minimum possible on-current in the config file. Various parameters from the transfer characteristics are saved as a spreadsheet along with standard error. These parameters include on current, off current, subthreshold slope and threshold voltage for the carbon nanotube devices, and on current, off current and major Dirac point voltage for graphene devices. The device type being analysed can be set in the config file.

The third module allows for comparison of transfer measurements taken of the same channel before and after some modification. It also calculates the shift in either threshold voltage or major Dirac voltage of the device.

### 1.3.2. Carbon Nanotube Network Devices

Each carbon nanotube device fabricated was electrically characterised as described in **?@sec-electrical-characterisation**, and electrical data was analysed using the Python code discussed in Section B.4. Devices with a 100 nm or 300 nm SiO<sub>2</sub> layer were used for liquid gated measurements, and devices with a 100 nm SiO<sub>2</sub> layer were used for backgated measurements. Figure 1.6 displays multi-channel measurements of representative devices fabricated as described in **?@sec-fabrication**. To ensure a consistent comparison, each device here was encapsulated with AZ® 1518 encapsulation before measurements were taken. The channels which did not exhibit reliable transistor characteristics are not shown. These ‘non-working’ channels were either shorted, due to metal remaining on the channel after lift-off, or were very low current, due to a very sparse carbon nanotube network. Devices shown here with a solvent-deposited carbon nanotube network were fabricated prior to Jan 2022; devices with a surfactant-deposited network without steam present were fabricated prior to Jun 2021; devices with a surfactant-deposited network without steam were fabricated prior to Sep 2022.

#### Liquid-Gated CNTFETs

The liquid-gated devices in Figure 1.6a, Figure 1.6c and Figure 1.6e each exhibited ambipolar characteristics, commonly observed in liquid-gated carbon nanotube network FETs [2], [27]–[31]. When devices were appropriately configured, leakage current (shown by the dashed traces) did not exceed  $\sim 1 \times 10^{-7}$  V across the forward and reverse sweep. The devices shown which used steam-deposited carbon nanotube films showed the least hysteresis. Section 1.2.1 demonstrates that the mean diameter of the bundles in these films is about 0.9 nm less than the mean bundles in films deposited without steam present, and 5.5 nm less than those in films deposited in solvent. Hysteresis is known to scale roughly linearly with bundle diameter, due to trapped charge increasing as bundle density of states is increased [32]. Steam-deposited devices also showed significantly less channel-to-channel variation in electrical characteristics more generally. Channel 1 in Figure 1.6a has a much higher off-current than the other channels of the same device,

### 1.3. Electrical Characteristics of Pristine Devices

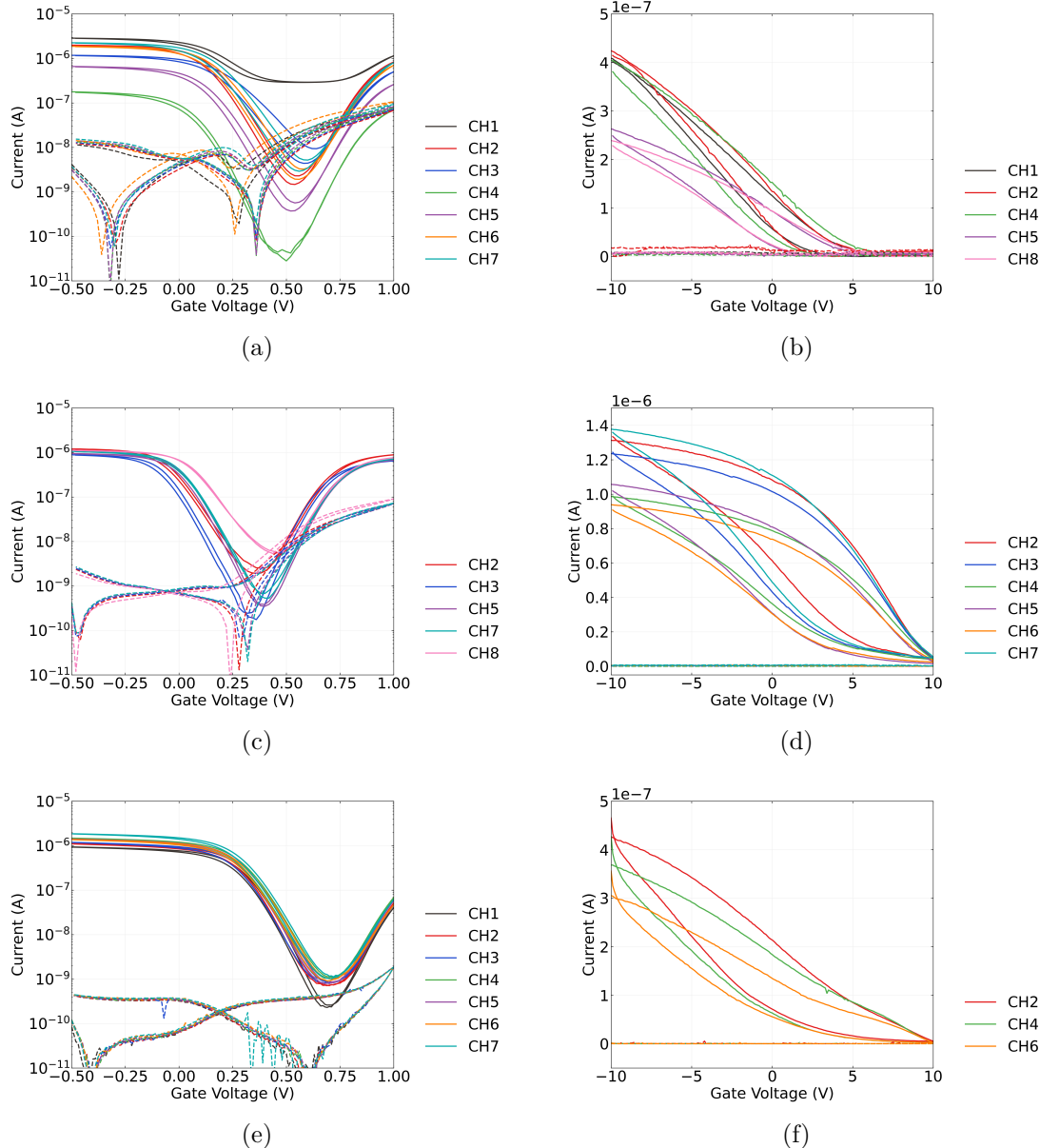


Figure 1.6.: Liquid-gated (left) and back-gated (right) transfer characteristics of AZ® 1518 encapsulated field-effect transistors, where the film was deposited with solvent in (a) and (b), deposited with surfactant in (c) and (d), and deposited with surfactant in the presence of steam in (e) and (f). A step size of 100 mV was used for the backgated sweeps in (a), (c) and (e), while a step size of 20 mV was used for the liquid-gated sweeps in (b), (d) and (f). Gate current (leakage current) is shown with a dashed line. The source-drain voltage used for all sweeps was  $V_{ds} = 100\text{mV}$ , and 1XPBS was used as the buffer for the liquid-gated measurements here.

1. Characteristics of Pristine Carbon Nanotube & Graphene Field Effect Transistors

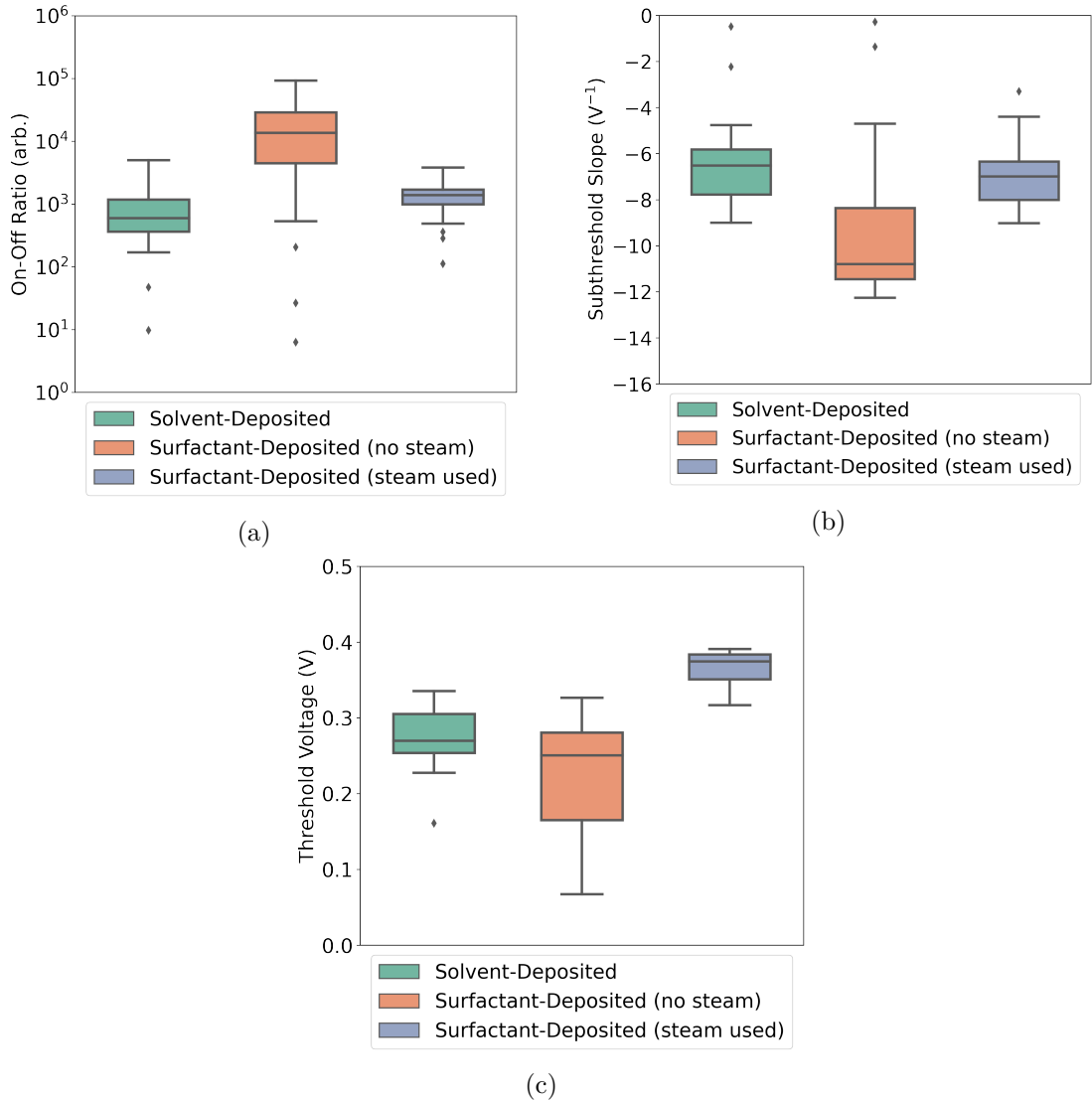


Figure 1.7.: These boxplots illustrate the statistical distribution of (a) the on-off ratio, (b) the subthreshold slope, and (c) the threshold voltage of AZ® 1518 encapsulated liquid-gated transistor channels corresponding to each type of carbon nanotube film deposition. For each deposition type, electrical characteristics were taken of 21 channels of at least three separate devices. The boxes indicate the 25th and 75th percentile of the distribution.

### 1.3. Electrical Characteristics of Pristine Devices

which appears to be due to a uncommonly high proportion of metallic carbon nanotubes present in the network conduction pathways of this channel [33], [34].

A summary of key parameters of pristine liquid-gated devices is shown in Figure 1.7. The full dataset consists of three sets of 21 liquid-gated transfer characteristics of working channels, with each set corresponding to the use of a particular method of carbon nanotube network deposition in the device fabrication. Measurements from at least three devices are included in each set. Each entry in the summary corresponds to the average of the specific parameter in the forward and reverse sweep direction. When steam was used for surfactant deposition of films, the resulting devices showed highly consistent channel-to-channel electrical properties. Since the carbon nanotube films on these devices are relatively dense, as seen in Figure 1.1e, the network should be well above the percolation threshold. As many carbon nanotube pathways connect across the channel in parallel, small variations in the network morphology have less of an impact on the overall channel behaviour [2]. Figure 1.3 and Table 1.2 indicate that the range of bundle sizes is relatively low in the steam-deposited films used in these devices, meaning the electrical behaviour of dominant conduction pathways is more spatially consistent. The repeatable subthreshold regime behaviour between channels seen for steam-deposited devices is a desirable attribute for reliable real-time multiplexed biosensing [27], [28], [35].

Channels from surfactant-deposited film devices usually showed a larger on-off ratio and subthreshold slope than those from solvent-deposited devices. Decreasing the ratio of gate-sensitive semiconducting carbon nanotubes to metallic nanotubes tends to decrease the on-off ratio [2], [10], [33], [34]. Section 1.2.2 seems to indicate there are more metallic nanotubes present in the surfactant-deposited films than in the solvent-deposited films. However, percolating conduction pathways dominate device behaviour and nanotube pathways across the channel with a lower degree of bundling are less likely to contain metallic tubes [2]. Therefore, the larger on-off ratio for surfactant-deposited film devices is likely a result of their reduced nanotube bundle size and reduced bundle size variation relative to other films, as discussed in Section 1.2. The larger subthreshold slope is likely due to increased mobility from a denser nanotube network in surfactant-deposited films [33], as seen in Figure 1.1e. A larger on-off ratio and subthreshold slope results in a larger change in conductance in response to changes in the transfer characteristic curve. Therefore, the larger on-off ratio and subthreshold slope of steam-deposited devices is desirable for improved sensor performance [27], [28], [35].

All channels characterised had a positive threshold voltage ( $V_{th}$ ). The threshold voltage was largest and most consistent for steam-assisted surfactant-deposited films. The relatively high values of  $V_{th}$  which correspond to channel measurements from steam-assisted surfactant-deposited devices indicates increased *p*-doping of the network relative to networks deposited via alternative processes [2], [36], [37]. As seen from Figure 1.2e-f and Figure 1.4c, the steam deposition process leads to the presence of significant, persistent surfactant aggregates. It has been previously established that residual surfactant can *p*-dope carbon nanotubes, alongside enhancing *p*-doping from adsorbed oxygen and

## 1. Characteristics of Pristine Carbon Nanotube & Graphene Field Effect Transistors

water [15], [22], [38]. The presence of residual surfactant may also explain the lowered subthreshold slope, and therefore mobility, of the steam-deposited devices relative to devices with films deposited in surfactant without steam. The analysis by Kane *et al.* shows that the thermal annealing at 150°C used in this work to remove residual surfactant is likely inadequate for this purpose. Oxidation of devices and vacuum annealing at high temperatures ( $> 600^\circ\text{C}$ ) may be required for effective desorption of the persistent surfactant [22], [39]. Devices using films made using the alternative two methods have the advantage of not requiring careful treatment to remove surfactant.

### Back-Gated CNTFETs

When characterising devices using the vapour delivery system chip carrier, the setup arrangement meant all measurements were taken using a backgate. Figure 1.6b, Figure 1.6d and Figure 1.6f show that backgated devices exhibit *p*-type transistor behaviour. Gate current leakage was negligible, as shown by the dashed line staying close to zero across the sweep. Significant hysteresis was observed. The hysteresis can be explained by the presence of defects or charge traps within and on the surface of the silicon dioxide and at interfaces between the silicon dioxide and carbon nanotubes [40]–[42]. The hysteresis observed was much greater than for the corresponding liquid-gated sweeps on the right. The devices fabricated with a solvent-based deposition were switched off at a lower voltage than the devices which used surfactant during deposition.

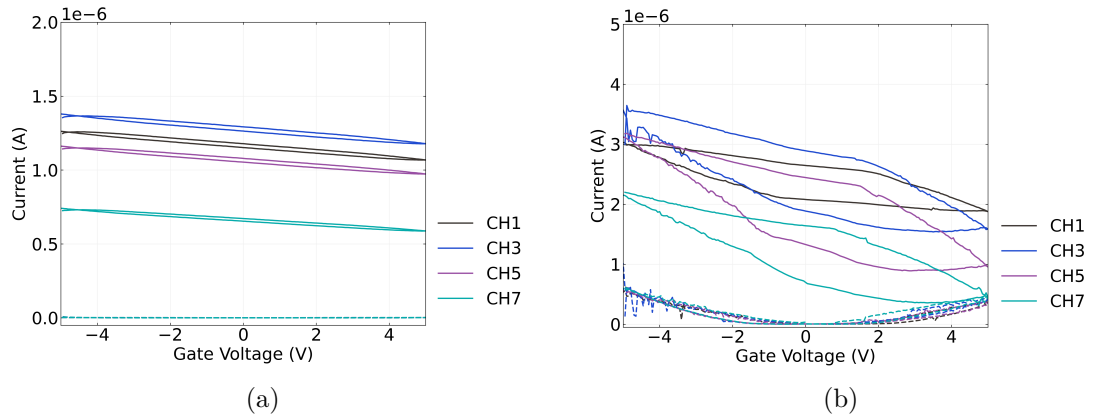


Figure 1.8.: Backgated transfer sweeps were taken of an single unencapsulated device with a 300 nm  $\text{SiO}_2$  layer and steam assisted surfactant-deposited carbon nanotube network channels before and after being covered in 50  $\mu\text{L}$  1XPBS electrolyte.

Transfer measurements were taken to determine whether backgated measurements could be taken of an unencapsulated device in the vapour sensor chamber with 1XPBS covering the channels. Figure 1.8 shows the behaviour of an unencapsulated backgated device with a 300 nm  $\text{SiO}_2$  layer before and after being covered by 50  $\mu\text{L}$  of 1XPBS (phosphate

### 1.3. Electrical Characteristics of Pristine Devices

buffered saline). The on-off ratio and hysteresis of the channels increase significantly. The presence of water increases hysteresis through introducing charge traps at the silicon dioxide surface around the carbon nanotubes and at the surface of the nanotubes themselves [40], [42]–[44]. There is also a significant increase in current leakage to the backgate for larger applied voltages, despite the electrolyte having no visible physical contact with the silicon backgate or copper plane. This leakage current may simply be due to an increase in relative humidity around the device due to the presence of water [45]. As any variation in threshold voltage due to hysteresis and significant leakage current are undesirable for sensing procedures, this configuration was not used for vapour sensing purposes.

#### 1.3.3. Graphene Devices

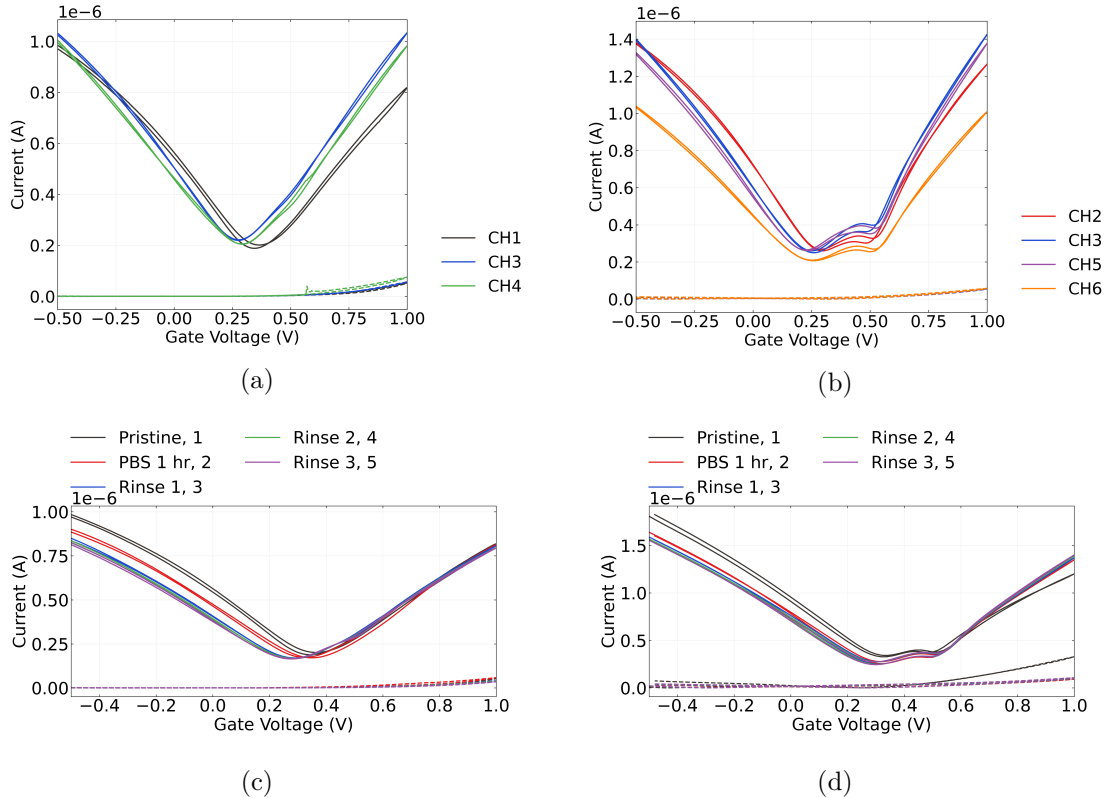


Figure 1.9.: These figures show liquid-gated transfer characteristics of channels from two AZ® 1518 encapsulated graphene devices. The characteristics of working device channels upon initial exposure to 1XPBS are shown in (a) and (b). The transfer characteristics of channel 1 in (a) and channel 5 in (b) after various degrees of exposure to 1XPBS are shown in (c) and (d) respectively, with each transfer sweep numbered in the order the sweeps were taken. The dashed lines correspond to measurements of gate leakage current.

## 1. Characteristics of Pristine Carbon Nanotube & Graphene Field Effect Transistors

Graphene field-effect transistor devices were electrically characterised in the manner described in ?@sec-electrical-characterisation and analysed using the Python code discussed in Section B.4.

Figure 1.9 shows the liquid-gated transfer characteristics of two graphene devices. These devices were fabricated prior to Jun 2021. Both devices exhibit the ambipolar characteristics typical of liquid-gated graphene devices [46]–[49]. As with the carbon nanotube network devices, leakage current remained below  $\sim 1 \times 10^{-7}$  V across both the forward and reverse sweep. Hysteresis between the forward and reverse sweep is caused by trapping of charge within and on the surface of the  $\text{SiO}_2$  dielectric [50]. The major Dirac point for these devices is slightly to the right of  $V_{\text{Dirac}} \approx 0$  V, which indicates *p*-doping of the channel. This slight *p*-doping is likely a result of a adsorption of oxygen and water from the air and residue resist from photolithography [49], [51], [52].

Some devices exhibited a double-minima feature, indicating the presence of two Dirac points. This effect arises due to doping of graphene by the metal contacts. In shorter length channels, metal doping affects the entire channel length, leading to a consistent Fermi level and a single Dirac point. However, for longer channel lengths like ours, the doping effect from metal contact no longer reaches the entire channel, leading to a difference in Fermi level between the graphene in the channel and graphene under the metal contact. The difference in Fermi levels results in the presence of a second Dirac point [50], [53], [54]. The global minimum of the transfer characteristic can be referred to as the ‘major’ Dirac point.

Figure 1.9 also shows the effect of 1XPBS on the graphene channels. The channels were measured on exposure to 1XPBS, after exposure to 1XPBS for one hour, and after the device surface was rinsed and 1XPBS was replaced in the well one time, two times and three times successively. A slight negative shift of the major Dirac point was observed. This effect is possibly a result of gate bias stress, where successive transfer sweeps introduce charge traps to the graphene layer and alters the current level at a given gate voltage [55], [56]. Alternatively, Kireev *et al.* found that a series of liquid-gated sweeps also reduced the size of the second Dirac point, and suggested that it indicated the gate current was removing atmospheric contaminants from the graphene surface via current annealing [49]. This could be explained as the removal of contaminants causing improved contact between the metal and graphene surface, and thus increasing metal doping and consistency of the Fermi level across the channel. If the contaminants removed are *p*-dopants, then this effect could also explain the negative shift of the major Dirac point.

#### 1.4. Aqueous Sensing of Phosphate Buffered Saline Concentration

Table 1.3.: Average on-off ratio and major Dirac point voltage for AZ® 1518 encapsulated liquid-gated graphene transistor channels at various stages of exposure to 1XPBS. Electrical characteristics were taken of 6 channels total, three channels from each of two devices.

	1XPBS: Initial	1XPBS: After 1 hr	1XPBS: Rinse
On-Off Ratio (arb.)	$5.1 \pm 0.3$	$5.0 \pm 0.7$	$5.0 \pm 0.6$
Dirac Point Voltage (V)	$0.28 \pm 0.04$	$0.31 \pm 0.03$	$0.28 \pm 0.02$

Table 1.3 shows the on-off ratio and major Dirac point voltage of the graphene devices. Apart from the previously-mentioned slight negative shift of the major Dirac point, these values were highly consistent before and after exposure to 1XPBS.

### 1.4. Aqueous Sensing of Phosphate Buffered Saline Concentration

#### 1.4.1. Control Series and Baseline Drift

Table 1.4.: The threshold voltages  $V_{th}$  of each working channel of a steam-deposited device, and the difference between each  $V_{th}$  and the mean device threshold voltage  $V_{th,mean}$ .

Channels	CH1	CH2	CH3	CH5	CH6	CH7
Threshold voltage (mV)	160	150	130	140	180	140
Relative to mean (mV)	10	0	-20	-10	30	-10

To verify the sensitivity of the fabricated field-effect transistors and therefore verify their suitability for sensing, control measurements replicating a typical sensing experiment were taken before functionalising the channels of a carbon nanotube network device. The first step to verifying device suitability was ensuring the device showed no response to 1XPBS. This sequence is referred to in this thesis as the ‘PBS control series’. The PDMS well contained  $80 \mu\text{L}$  1X PBS at 0 s. The PBS control series ran over the first 1800 s, with  $20\mu\text{L}$  phosphate buffer saline (1XPBS) additions at 100 s, 200 s and 300 s, and  $20\mu\text{L}$  subtractions at 400 s, 500 s and 600 s. The device was left untouched over the next 1200 s to allow the current level to settle. The gate voltage was held at  $V_g = 0$  V.

Figure 1.10a shows the transfer sweeps of the six working channels of a steam-assisted surfactant-deposited carbon nanotube field-effect transistor measured using the NI PXIe.

## 1. Characteristics of Pristine Carbon Nanotube & Graphene Field Effect Transistors

The device was fabricated on a substrate with a 300 nm SiO<sub>2</sub> layer, the carbon nanotube film was deposited using the steam-assisted surfactant method and encapsulated with AZ® 1518 before measurement. The central feature in the transfer characteristics of channels 1 and 7 are absolute-value measurements of negative current. These are unphysical measurements due to equipment error, and can be considered as regions where zero current passes through the channel. The threshold voltages of the channels are shown in Table 1.4. Table 1.4 also shows the difference between the threshold voltage of each channel and the mean threshold voltage of the device. The mean threshold voltage was  $V_{th} = 150 \pm 20$  mV. As discussed previously, the electrical characteristics are highly consistent between the channels due to the film deposition method used.

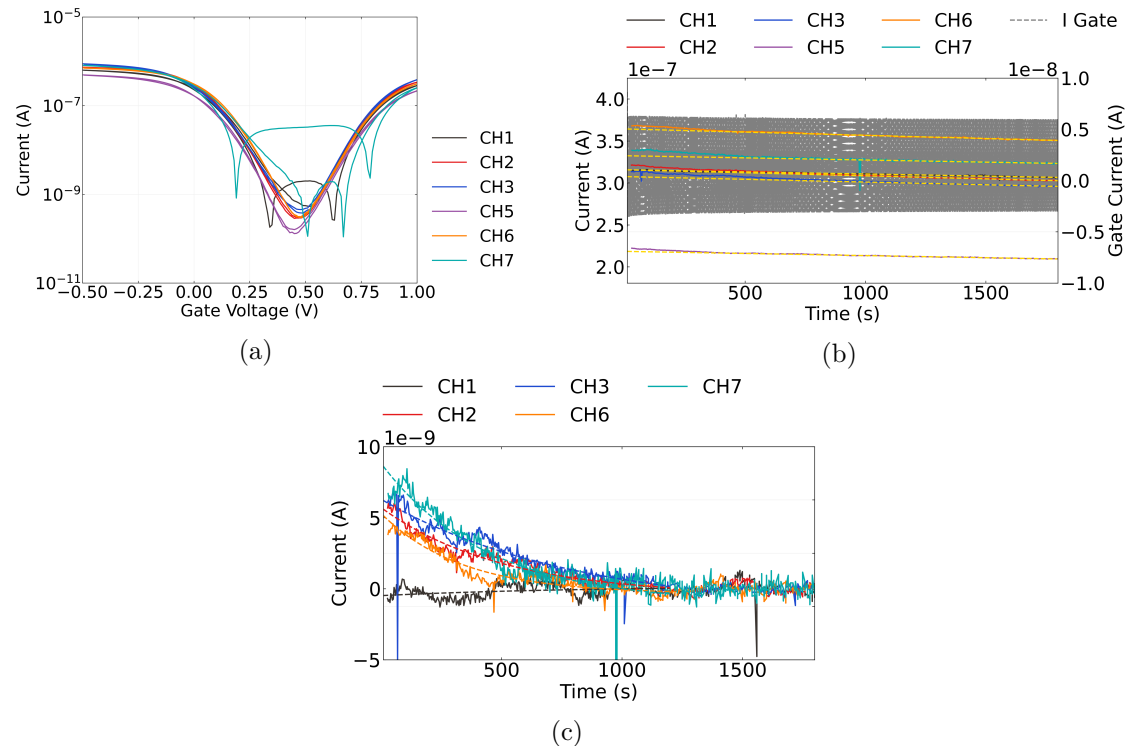


Figure 1.10.: The transfer characteristics in (a) were taken of the steam-deposited carbon nanotube field-effect transistor used here for an example of salt concentration sensing. The absolute values of measurements are shown, so that negative values resulting from measurement error can be visualised. Linear fits to the PBS control series from each channel from 1200 s onwards are shown in (b), while exponential fits to the PBS control series from 0 – 1200 with the linear fit subtracted are shown in (c). No significant response to PBS additions are seen at any of the addition times from 100 s - 600 s.

Figure 1.10b shows the PBS control series corresponding to each device channel alongside gate current. In both series, there is no clear stepwise response to any addition or subtraction of 1XPBS. Gate leakage current remains negligible across the entire control

#### 1.4. Aqueous Sensing of Phosphate Buffered Saline Concentration

series, with no change in response to 1XPBS additions. The current has a period of faster decay followed by slower baseline drift, similar to observations by Lin *et al.* and more recently Noyce *et al.* for parallel arrangements of single carbon nanotubes in air or vacuum [56], [57]. This effect results from changes in the occupancy of charge traps in and around the substrate and carbon nanotubes. The magnitude of baseline drift is lower for our devices than for those characterised by Noyce *et al.*, which may be a result of numerous device and setup differences which affect the presence of charge traps. These differences include liquid-gating instead of back-gated, the use of a network of carbon nanotubes instead of single nanotubes, a different channel length, the use of a 300 nm instead of 90 nm SiO<sub>2</sub> layer, and the use of an asymmetric, liquid-gated transfer sweep over a shorter voltage range to characterise devices before each control series was measured [56].

Table 1.5.: The coefficients of linear fits to the PBS control series of each channel between 1200 – 1800 s, where  $c_1$  is the gradient and  $c_2$  is the constant term.

Channels	CH1	CH2	CH3	CH5	CH6	CH7
$c_1$ (pA/s)	-5.1±0.2	-7.2±0.1	-6.5±0.1	-5.0±0.1	-7.6±0.1	-5.1±0.2
$c_2$ ( $\mu$ A)	0.316	0.316	0.308	0.218	0.364	0.332

Table 1.6.: The coefficients of exponential fits to the PBS control series of each channel between 0 – 1200 s, after the linear fit has been subtracted, where  $I_0$  is the gradient and  $\tau$  is the time constant.

Channels	CH1	CH2	CH3	CH6	CH7
$I_0$ (nA)	-0.66 ± 0.26	6.21 ± 0.09	7.84 ± 0.41	5.67 ± 0.11	9.82 ± 0.47
$\tau$ (s)	800 ± 750	500 ± 30	790 ± 100	330 ± 20	440 ± 70

As a first approximation to the longer time constant exponentials discussed by Noyce *et al.* [56], linear fits were performed on each PBS control series from 1200 – 1800 s. These linear fits are shown by the dashed yellow lines in Figure 1.10b. The parameters from each fit in Figure 1.10b are shown in Table 1.5, where  $I = c_1 t + c_2$ . The fits for channels 1, 5 and 7 are all in parallel within error. The gradient value for each fit in Figure 1.10b is reasonably consistent between all channels, all falling within a 2.6 pA/s range. When the long-term linear fits were subtracted from the raw data, the remaining dataset followed a exponential decay trend for both control series.

Figure 1.10c shows exponential fits to the remaining curve from 0 – 1200 s, which was successful for all channels except channel 5. The parameters from each fit are shown in Table 1.6, where  $I = I_0 \exp(-t/\tau)$ . Any constant term  $I_C$  resulting from the fit

## 1. Characteristics of Pristine Carbon Nanotube & Graphene Field Effect Transistors

was negligible and so could be neglected. The exponential fits had characteristic time constants  $\tau$  ranging between 300–800 s. This result indicates 1800 s is a sufficient length of time for this short-term baseline drift to decay almost completely for the channels with smaller time constants. However, it means that for some channels, a control sequence of up to 4000 s may be required for this term to be neglected. The exponential term for channel 1 has a amplitude close to zero, indicating the channel has low net trapped charge. It is unclear why the behaviour of this channel is significantly different from the others.

From this analysis it appears that the baseline drift for the liquid-gated carbon nanotube devices can be accurately approximated as a combination of a exponential and linear term. The lack of response to 1XPBS at any of the six PBS addition and removal times gives us confidence that this is a stable baseline which can be used for reliable chemical sensing. Furthermore, after  $\sim$  800 s the baseline drift can be reasonably approximated as linear, with a small gradient of less than -10 pA/s. The slow change of current means that it becomes easier to distinguish responses due to analyte addition. It can therefore be concluded that the 1800 s length of the PBS control series is appropriate for minimising baseline drift for more reliable sensing.

### 1.4.2. Sensing Series

A salt concentration sensing series were performed from 1800 s onwards, directly after the PBS control series. The responses to successive dilutions of the liquid-gate electrolyte were recorded to confirm the fabricated devices were sensitive to small environmental changes in their pristine state, to check for spurious signals, and to ensure gate current leakage or other confounding factors were not contributing to sensing responses. The PDMS well contained 80  $\mu$ L 1X PBS at 1800 s. During the series, successive additions of deionised water were made to reduce the concentration of PBS in the well. An initial 1X PBS addition was performed at 2100s, to confirm no changes occurred during the PBS control series that would interfere with sensing. All additions to the well in the sensing series and resulting changes to the PBS concentration in the well are shown in Table 1.7.

Table 1.7.: This table shows the times at which 20  $\mu$ L additions were made to the PDMS well, with 300 s between each addition. The concentration in the well after each addition and the change in concentration after each addition are also shown. The well contained 80  $\mu$ L of 1X PBS at 1800 s.

	1X PBS Addition	DI Water Additions				
Time (s)	2100	2400	2700	3000	3300	3600
Final PBS volume ( $\mu$ L)	100	120	140	160	180	200
Final PBS concentration	1X	0.83X	0.71X	0.63X	0.56X	0.50X

#### 1.4. Aqueous Sensing of Phosphate Buffered Saline Concentration

$\Delta$ PBS concentration	0	-0.17X	-0.12X	-0.09X	-0.07X	-0.06X
----------------------------	---	--------	--------	--------	--------	--------

Figure 1.11a shows a multiplexed salt concentration sensing series from the channels of a single AZ® 1518 encapsulated device, measured with the NI-PXIe. The gate voltage used was 0 V, which meant current measurements were well above the magnitude of the subthreshold device current. Gate current measurements did not exceed 1 nA for the SU8 encapsulated devices, and did not exceed 10 nA for the AZ® 1518 devices. At each of the deionised water addition times, the current traces for at least two out of six channels showed a sharp, transient increase in current followed by a return to an increased baseline. It is well established that changing the salt concentration of the liquid gate has an electrostatic gating effect on the carbon nanotubes or graphene, and changes the transfer characteristics of the channel. This shift in transfer characteristic leads to a real-time signal response to each addition [28], [47], [49].

Using the data in Table 1.5, the linear term approximating baseline drift ( $c_1 t$ ) for each channel can be subtracted from the data in Figure 1.11a to account for the downward drift. The mean current level just before 1800 s then becomes roughly constant. Next, each channel is normalised relative to their initial mean current level  $I_0$ . Artifacts resulting from PXIE-2737 module lag, single datapoints which fall well below the current level of the immediately preceding and succeeding datapoints, are also removed. This ‘despike’ process uses an interquartile range filter, which is described in Section 1.3.1. The resulting dataset is shown in Figure 1.11b. This figure shows that the signal-to-noise ratio remains roughly similar across all channels of the device. However, the behaviour of the initial transient increase with each addition is highly variable across channels and between additions for a single channel.

As measurement of the highly variable initial transient is not useful for robust sensing purposes, a moving median filter was applied, with the implementation of this filter discussed in Section 1.3.1. The filtered data is shown in Figure 1.11c. Noise and initial transients are removed completely, while the clearly defined step to a new current baseline is retained. Using the realtime data in Figure 1.11c, a plot of signal against addition can be created using the method described in Section 1.3.1, shown in Figure 1.11d. This presentation of the data allows us to see the increase at each step relative to  $I_0$ .

Intriguingly, even though the largest change in PBS concentration occurred at the first deionised water addition (see Table 1.7), there was very little signal change across all channels, while a relatively large change occurred at the second addition. The logarithm of final salt concentration has previously been shown to be proportional to conductance change in the linear on-regime [47]. Figure 1.11e shows the signal change presented in terms of this logarithmic relationship. The median values of the first two additions do not line up well with the overall logarithmic trend; insufficient mixing in the tightly enclosed PDMS well environment for the first few additions may be responsible for this result. Subsequent additions may improve mixing in the well, leading to the change

## 1. Characteristics of Pristine Carbon Nanotube & Graphene Field Effect Transistors

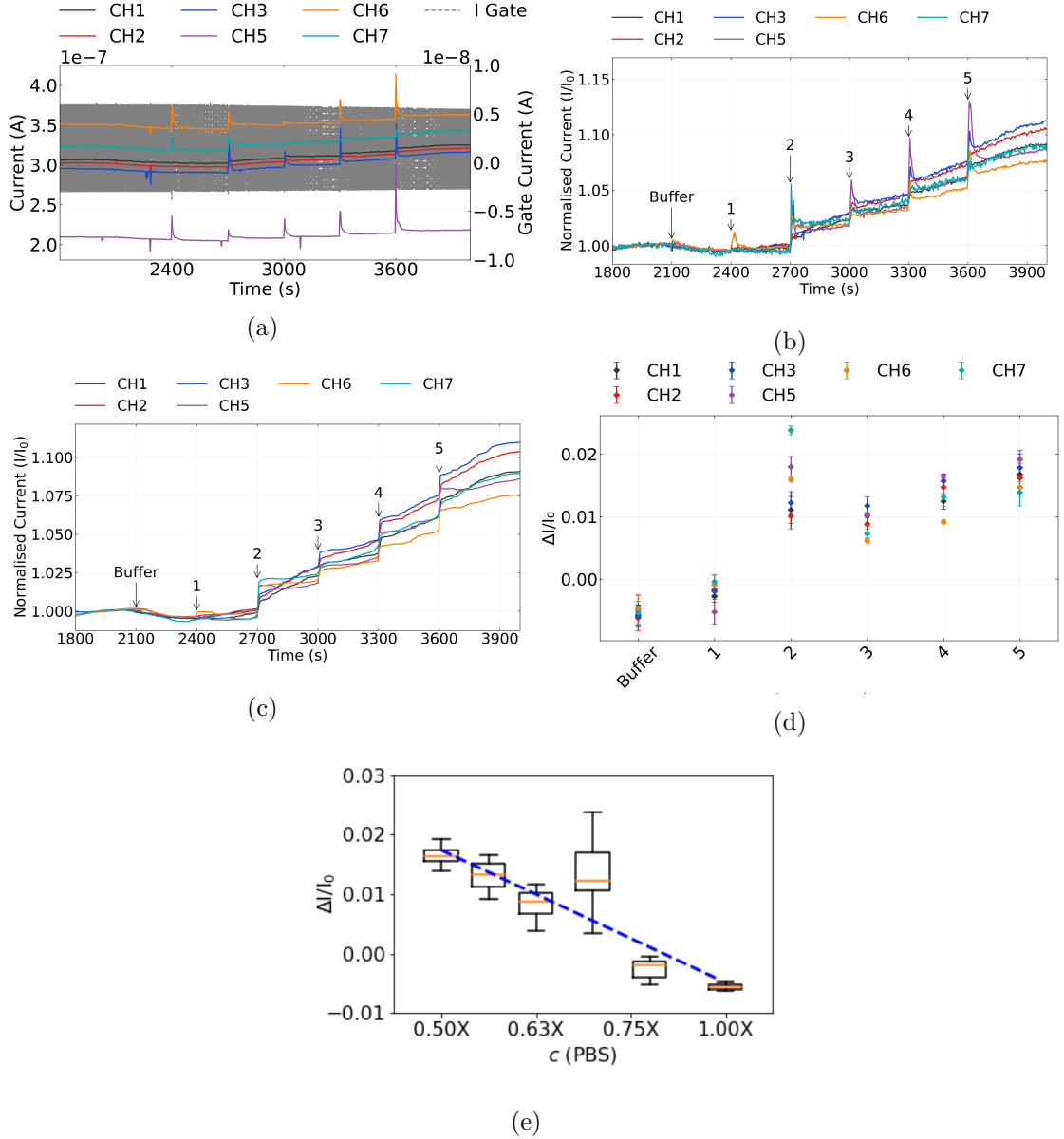


Figure 1.11.: Various visualisations of a multiplexed salt concentration sensing series taken from a single device. The source-drain voltage  $V_{ds}$  was 100 mV, and gate voltage  $V_g$  was 0 V. In (a), the raw current measurements for each channel are shown alongside gate current. The same measurements after despiking, removal of baseline drift and normalisation to initial current are shown in (b), (c) shows the data in (b) after being processed with a moving median filter, and (d) shows the signal changes in (c). The signal data in (d) is shown in box plot format in (e) alongside a fit to the median change in signal for each addition. The R squared value for the fit was 0.86.

#### 1.4. Aqueous Sensing of Phosphate Buffered Saline Concentration

in concentration at the surface of the channel being more representative of the overall concentration in the well.

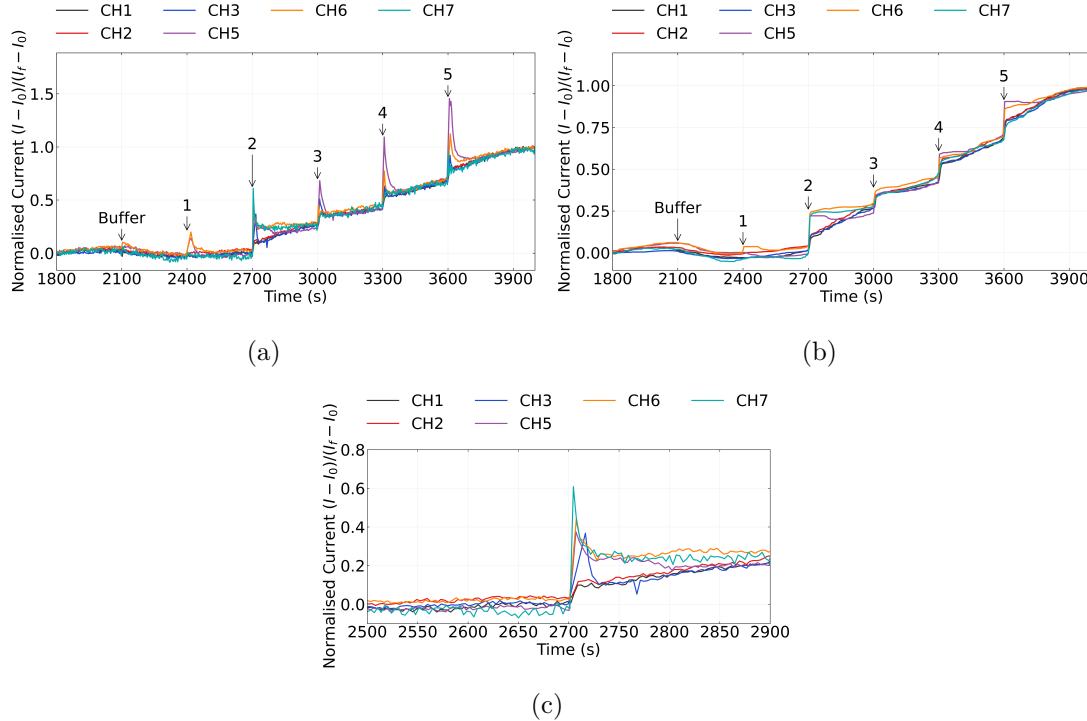


Figure 1.12.: The processed data shown in Figure 1.11b and Figure 1.11c is normalised to  $I_0$ , but an alternative normalisation can more effectively filter out remaining drift present. This normalisation presents data relative to both  $I_0$  and the final current reading  $I_f$  using the formula  $(I - I_0)/(I_f - I_0)$ . Using this normalisation, the data in Figure 1.11b and Figure 1.11c can be displayed instead as (a) and (b) respectively. (c) shows a magnified version of the step at addition 2 in (a).

In Figure 1.11b and Figure 1.11c, from around the second deionised water addition onwards, the drift behaviours of individual channels begin to significantly diverge. This deviation from the baseline drift subtracted from the raw data occurs either because the linear fit is only a first-order approximation which weakens with time, or because the additions themselves affect the drift behaviour. Displaying the data as discrete signal changes, as in Figure 1.11d, is one way of excluding these deviations (see Section 1.3.1). An alternative way of presenting the signal changes, by normalising relative to both  $I_0$  and the final current reading with the formula  $(I - I_0)/(I_f - I_0)$ , is shown in Figure 1.12. This approach is useful for filtering out remaining unaccounted-for drift behaviour in order to compare the short-term transient responses to additions across the device channels. Furthermore, it lets us better understand how the short-term transient responses affect the longer-term step responses discussed earlier.

## 1. Characteristics of Pristine Carbon Nanotube & Graphene Field Effect Transistors

Figure 1.12a and Figure 1.12c show that the transient responses to DI water additions vary significantly across the surface of the device. For example, Figure 1.12c shows that in response to the second DI water addition, channel 7 gives a large initial transient response about twice the size of the step increase between 2600 and 2800 s. Meanwhile, channels 1 and 2 show no transient response above the step increase. Figure 1.12c indicates transient size is based on location across the device, with neighbouring channels showing the most similar behaviour. This spatially-dependent behaviour may indicate transient responses are determined by the location of the channel relative to either the location of water additions or the slightly-variable location of the liquid gate. Larger and longer-lasting transient responses are not entirely removed by the moving median filter, as shown by comparing Figure 1.12a to Figure 1.11c, and so careful placement of additions is important when sensing to minimise this effect. However, even the longest-lasting transients appear to decay to zero within about 200 s, demonstrating that a 200 s spacing between additions at minimum is necessary for reliable real-time liquid-gated sensing using this setup.

### Signal-to-Noise Ratio

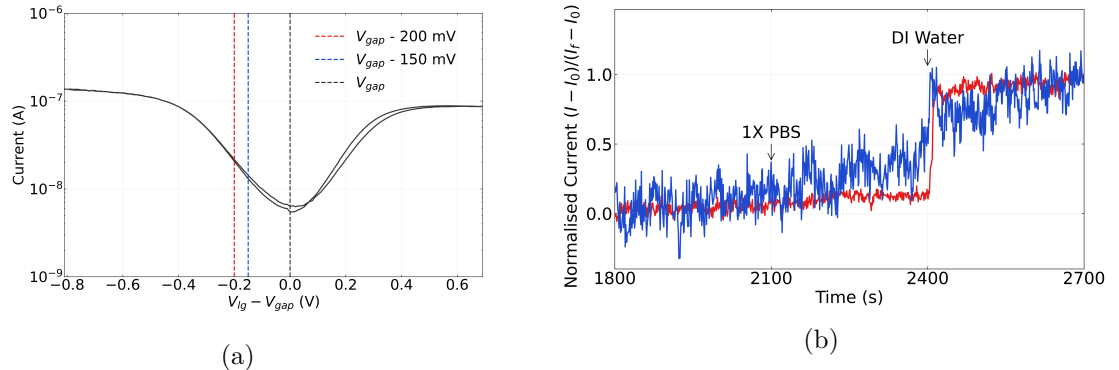


Figure 1.13.: The transfer characteristics of a single steam-deposited carbon nanotube field-effect transistor channel are shown in (a).  $V_{gap}$  is the gate voltage corresponding to the center of the transistor bandgap, found at the minimum of the characteristic curve. The signal-to-noise ratio of the channel response to a deionised water addition after a suitable control series is shown in (b). The blue current trace in (b) was performed gating the device 150 mV away from  $V_{gap}$ , while the red current was performed gating the device 200 mV away from  $V_{gap}$ .

To understand the effect of gate voltages on signal-to-noise ratio, two PBS control and salt concentration sensing series were performed with the same channel at different gate voltages. The transfer characteristics of this channel are shown in Figure 1.13a, with coloured dashed lines marking the voltages used for gating the transistor during each sensing series. Figure 1.13 shows the initial PBS and DI water additions made after

## 1.5. Vapour Sensing with Ethyl Hexanoate

1800 s. Previous work on the signal-to-noise ratio for liquid-gated, encapsulated carbon nanotube devices suggests that gating devices close to  $V_{gap}$  should give the largest signal-to-noise ratio for salt concentration additions [28]. However, this was not what was observed for our carbon nanotube field-effect transistor, as Figure 1.13 shows improved signal-to-noise ratio, i.e. the signal step can be more clearly distinguished, when gated at a voltage further removed from  $V_{gap}$ . This discrepancy could be a result of the use of a network of carbon nanotubes rather than a single nanotube; gating may have less of an impact on noise when a network morphology is used. Alternatively, it could be a result of a lack of mixing in our static well setup leading to inconsistent signal sizes with concentration change. Heller *et al.* used a flow cell during their signal-to-ratio work [28]. By using a flow cell with our devices, it would be possible to confirm whether this is the case, and this might also help us reduce the size of unwanted transient responses resulting from drop-wise additions.

## 1.5. Vapour Sensing with Ethyl Hexanoate

### 1.5.1. Baseline Drift

When sensing vapour in the vapour delivery system, devices have no liquid gate and are instead backgated when taking measurements. Therefore, the baseline drift of devices characterised in this manner should be considered separately to those characterised in an liquid-gated environment. Device baseline drift of a backgated device in the vapour sensing chamber is therefore examined here in more detail. A AZ® 1518 encapsulated carbon nanotube network device was used in this discussion. The device was fabricated on a substrate with a 300 nm SiO<sub>2</sub> layer, and the carbon nanotube film was deposited using the steam-assisted surfactant method. Before measurements were taken, the vapour system was purged of vapour, the total dilution flow into the chamber was set at 200 sccm as read by the Tylan mass flow controller and flow to the PID was set to 150 sccm on the flowmeter. The transfer sweep of a channel on this device (channel 6) is shown in Figure 1.14, measured using the B1500A semiconductor device analyser.

Figure 1.15 (a) shows 3600 s of baseline drift from the same channel when the device was backgated at  $V_g = 0$  V and a source-drain voltage of  $V_{ds} = 100$  mV was placed across the channel. During this period of time, a 200 sccm nitrogen flow was placed through the device chamber with the dilution mass flow controller. Gate leakage current remains negligible across the entire control series. As seen for the liquid-gated device in Section 1.4.1, there is a period of rapid exponential decay followed by a period of stable, approximately linear baseline drift. The baseline drift observed here appears to be significantly lower than that seen by Noyce *et al.* [56]. This observation suggests that the higher magnitude of drift observed by Noyce *et al.* is not a result of backgating in air, as previously suggested, but instead due to the use of a significantly different fabrication process for their devices.

## 1. Characteristics of Pristine Carbon Nanotube & Graphene Field Effect Transistors

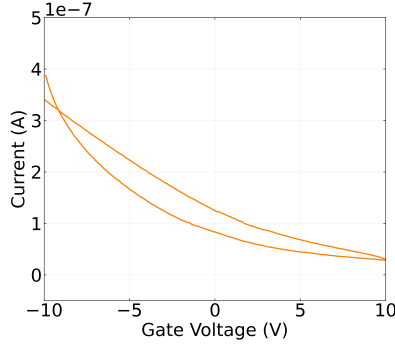


Figure 1.14.: Transfer sweep of a steam-deposited carbon nanotube network field-effect transistor, backgated in the vapour delivery system device chamber.

A linear least-squares fit was performed on the samples taken between 2400 s – 3600 s, and the fit obtained had an R-squared value of 0.998. The constants obtained for the linear fit, where  $I = c_1 t + c_2$ , were  $c_1 = -17.31 \pm 0.05 \text{ pAs}^{-1}$  and  $c_2 = 0.779 \mu\text{A}$ . Both linear and constant terms are slightly higher than that of the average liquid-gated device drift. The linear fit was then subtracted from the raw data, and an exponential least-squares fit was performed on the remaining dataset. Figure 1.15 (b) shows the exponential fit to this remaining dataset from 0 s – 3600 s, where the R-squared value was 0.89. The constants obtained for the exponential fit  $I = I_0 \exp(-t/\tau)$  were  $I_0 = 7.20 \pm 0.05 \text{ nA}$  and  $\tau = 730 \pm 10$ . The exponential term is very similar in size and time constant to those of the liquid-gated device, which may indicate this decay behaviour is independent of the type of transistor gating. The large time constant indicates that 3600 s is just sufficient for the exponential term to decay to approximately zero before starting a sensing series for this channel.

This analysis indicates that the baseline drift for the backgated carbon nanotube under nitrogen flow can be approximated as a combination of a exponential, linear and constant term. Furthermore, while only measured here for a single channel, it appears likely that we can expect backgated baseline drift behaviour to be similar to the multiplexed liquid-gated drifts observed in Section 1.4.1. It seems that the nature of baseline drift in these devices is largely a result of the general nature of the carbon nanotube network, rather than the type of gating used for device characterisation.

### 1.5.2. Sensing Series

Directly after the 3600 s control series, the device was exposed to four intervals of ethyl hexanoate vapour flow from the carrier line. 5 mL of ethyl hexanoate was placed into the analyte bottle on the carrier line before testing for the sensing series. The same settings for the vapour delivery system were kept from Section 1.5.1. A total flow of 200 sccm between the two mass flow controllers was kept through the chamber at all times. During each interval 150 sccm flow was placed through the carrier line. Apart

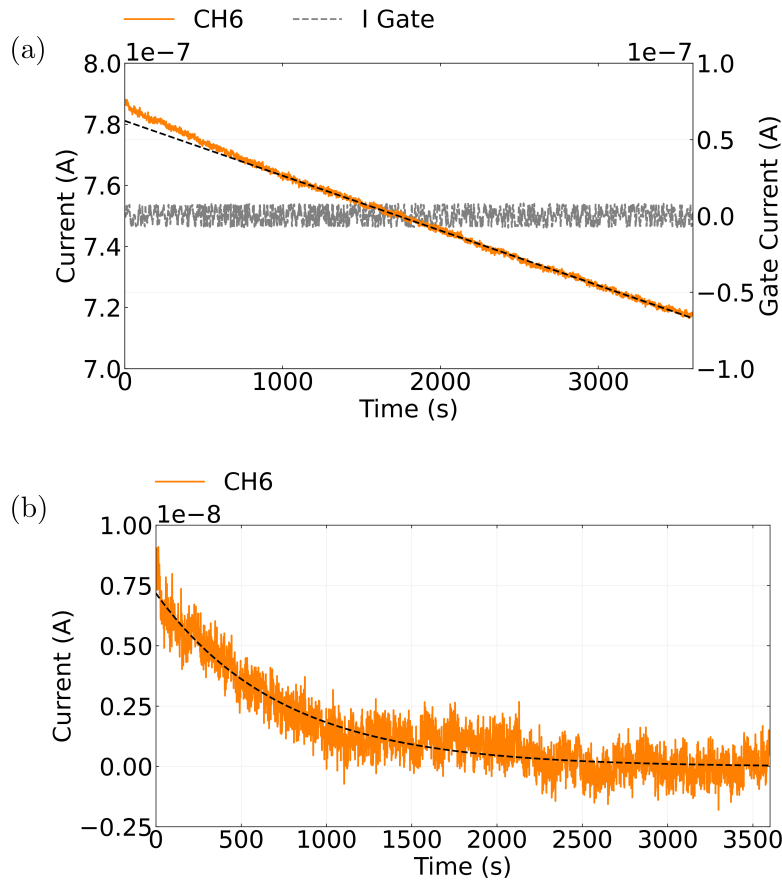


Figure 1.15.: The source-drain and gate current measured for a backgated device channel across 3600 s, where  $V_d s = 100$  mV and  $V_g = 0$  V is shown in (a). A linear fit to the data from 2400 s onwards has been indicated on (a) with a black dashed line. The linear fit has then been subtracted from (a) to give the dataset shown in (b). An exponential fit to the dataset in (b) is also shown in black. The R-squared value for the linear fit in (a) was 0.998, while the R-squared value for the exponential fit in (b) was 0.89.

## 1. Characteristics of Pristine Carbon Nanotube & Graphene Field Effect Transistors

for the duration of these intervals, flow through the carrier line was kept at zero. The intervals were of varying lengths to see how the carbon nanotube device responded to various concentrations of vapour in the chamber as recorded by the PID. A 1200 s recovery period was placed between each carrier flow interval, where 200 sccm flow was placed into the chamber from the dilution line. A separate test was also performed in an identical manner, except no ethyl hexanoate was placed into the analyte bottle. The chamber temperature was  $22^{\circ}\text{C} \pm 2^{\circ}\text{C}$  for all measurements.

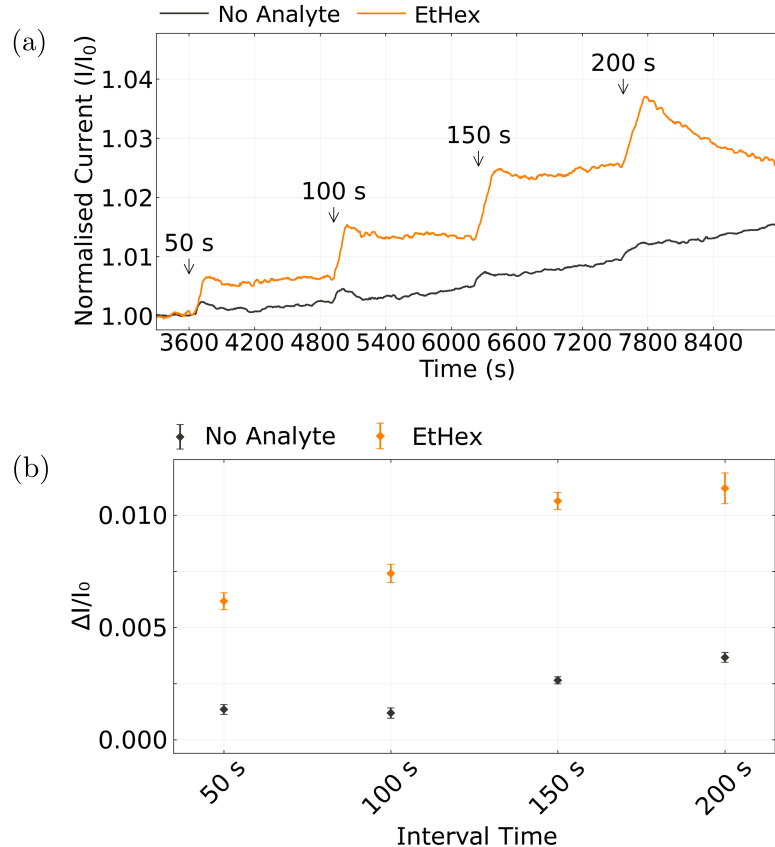


Figure 1.16.: Device channel responses to intervals of flow from the carrier line into the vapour delivery system chamber. Intervals begin at 3600 s, 4850 s, 6150 s and 7500 s. The length of each interval is indicated above the corresponding normalised current responses in (a) for both ethyl hexanoate (EtHex) and for no analyte present in the analyte bottle. The signal changes corresponding to the current responses to each interval for both ethyl hexanoate and for no analyte present are shown in (b).

Figure 1.16 shows the result of these interval tests, both with and without ethyl hexanoate placed in the analyte bottle. The data presented in Figure 1.16 (a) has been normalised, despiked, filtered and corrected for baseline drift in the manner described

### 1.5. Vapour Sensing with Ethyl Hexanoate

in both Section 1.3.1 and Section 1.4.2. Each interval of exposure to carrier line flow corresponds to a current increase. These increases have been labelled with the length of the corresponding interval used. When ethyl hexanoate is present in the analyte bottle on the carrier line, the response to each exposure interval is considerably larger than the response when no analyte is present. It should be noted that some response to carrier line flow is observed even when the analyte bottle is empty. This is most likely to be the result residual analyte in the carrier line being pumped into the chamber. It appears very low levels of analyte persist in the line even after purging the system lines with a roughing pump. Concentration measurements taken using the photoionisation detector, shown in Figure 1.17, also indicate some low-level, residual vapour reaches the chamber during each interval even when the analyte bottle is left empty.

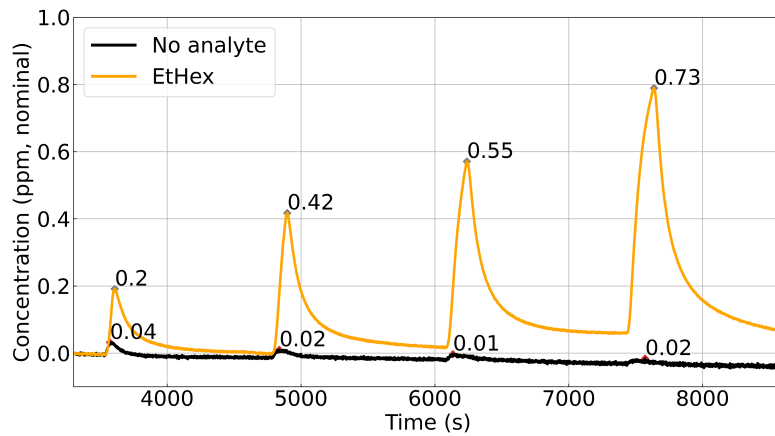


Figure 1.17.: Nominal concentration measurements by the photoionisation detector taken from the device chamber during device current sampling from 3600 s onwards, both with and without ethyl hexanoate (EtHex) in the analyte bottle. The maximum nominal concentration reached during each carrier flow interval is indicated above each peak.

The signal response seen corresponds to a change in conductance of the exposed carbon nanotubes within the device channel. These conductance changes occur due to the molecular adsorption of ethyl hexanoate vapour onto the external and internal surfaces of the nanotubes. The vapour can dope the semiconducting carbon nanotubes in the channel, causing a shift in the channel threshold voltage, and can cause carrier scattering when adsorbed onto the metallic nanotubes present. Binding of analyte to a gas sensing material can be reversible or irreversible. In general, adsorption onto carbon nanotube sensors is irreversible. This irreversibility means after a response to analyte, readings from the sensor will not return to the original baseline within the same timescale as the sensing response, even after stopping analyte flow to the chamber [58], [59]. From Figure 1.16, it is clear that the carbon nanotube sensor configuration used here is primarily irreversible, where the current level does not return to baseline within a period of 1200 s after analyte exposure.

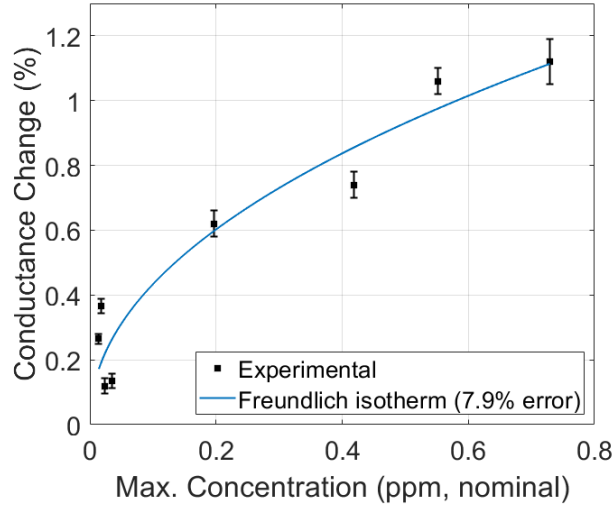


Figure 1.18.: Device response against maximum concentration measurement corresponding to each interval of carrier flow. The experimental results have been fitted with two adsorption isotherm models. The chamber temperature was  $22^{\circ}\text{C} \pm 2^{\circ}\text{C}$  across both datasets.

Assuming that the signal response is directly proportional to the degree of surface coverage by adsorbed analyte on the carbon nanotube network [59], it should be possible to model the relationship between signal response and concentration in the device chamber with an adsorption isotherm [58]. Figure 1.18 shows the maximum nominal concentration measured for every peak shown in Figure 1.17 plotted against the corresponding signal responses shown in Figure 1.16 (b). The Freundlich adsorption isotherm (Equation 1.1) models adsorption onto a heterogeneous surface.  $K_F$  is the adsorption capacity and  $1/n$  is adsorption intensity.  $1/n$  can be used to understand the heterogeneity of adsorbate sites [60], [61]. The vapour response factor is denoted as  $k_{RF}$ , which is equal to 1.6 for a 10.6 eV photoionisation detector (PID). As the PID has been run uncalibrated, a factor  $k_D$  has been included to account for linear span drift. As span drift due to window contamination can cause concentration readings to be reduced up to 30% after six months of PID operation, it is expected that  $k_D$  falls within the range of 0.2 – 1 [62], [63].

$$q_e = K_F(k_D k_{RF} C_e)^{1/n} \quad (1.1)$$

The best-fit Freundlich isotherm is shown alongside the experimental data in Figure 1.18, fitted using linear least-squares methods with an R-squared value of 0.921. The fitted isotherm had a value for  $n$  of  $n = 2.1 \pm 1.1$ . The isotherm has previously been used to model adsorption of volatile organic molecules onto single-walled carbon nanotubes. A value for  $n$  below  $\sim 5$  indicates the carbon nanotube network morphology used here has a relatively high maximum adsorption capacity. This results from using a nanotube network with a relatively high external surface area [58].

## 1.6. Conclusion

To ensure fabricated transistors were suitable for biosensing purposes, the morphology and electrical properties of the pristine carbon nanotube and graphene transistors were investigated.

The morphology of the carbon nanotube networks were found to have a significant impact on the electrical characteristics of the devices, which was determined through comparison of the skew-normal height profile of the carbon nanotube network and the key electrical parameters of a range of carbon nanotube devices. When networks were highly bundled ( $> 90\%$ ), there was a large range of carbon nanotube bundle diameters present in the network. This large variation in the size of conducting pathways resulted in a wide range of on-off ratios and threshold voltages for the liquid-gated devices created using these carbon nanotube films. In contrast, devices using films fabricated with a relatively low percentage of bundling ( $< 75 \%$ ) showed highly consistent on-off ratios and threshold voltages, along with low hysteresis, due to the relatively consistent bundle diameters and high density of these networks. These low-bundling networks were found to have a mean bundle distribution height of  $3.3 \pm 1.0$  nm. When performing multiplexed sensing, consistent channel behaviour is highly desirable since comparing sensing behaviour between channels is more straightforward.

However, atomic force microscope imaging and Raman spectroscopy also indicated that less bundled networks had the most surface contamination present. Aggregated surfactant present on the surface had a height of more than 4 nm, and introduced significant defects to the carbon nanotube network. The introduction of *p*-dopants to the carbon nanotubes by surfactant appears to have significantly increased the threshold voltage of steam-assisted surfactant-deposited network devices relative to steam-free surfactant-deposited network devices. Since the presence of surfactant could negatively impact biosensing, techniques to remove contaminants should be explored in more detail. Oxidation and thermal annealing of carbon nanotube films at high temperatures could be used to resolve this issue, and this is discussed further in [?@sec-future-work](#). The presence of electrolyte on the surface of a backgated transistor for use in vapour sensing was also found to significantly adversely affect its electrical characteristics.

Constant voltage real-time measurements of the carbon nanotube field-effect transistor devices had a characteristic drift that could be modelled using a exponential and linear term. The linear term of baseline drift had a reasonably consistent gradient between device channels, with a mean value of  $-6.1 \pm 1.2$ , indicating that similar drift behaviour should be reproducible between devices fabricated in the same manner. The time constant of the exponential term ranged from  $\tau = 330 \pm 20$  s to  $\tau = 800 \pm 750$  for the device characterised. These results indicate that the PBS control series is asuitable time length for minimising the effects of baseline drift on sensing, since the range of time constants are all well below the total timescale of the control series.

## *1. Characteristics of Pristine Carbon Nanotube & Graphene Field Effect Transistors*

Salt concentration or PBS dilution sensing series indicated that the carbon nanotube transistor devices were highly sensitive to environmental changes and therefore suitable for sensing work. Successive additions of deionised water to the 1XPBS present in the well gave signal responses of up to 2.5 % above the control response. The signal response was found to be proportional to the logarithm of concentration, giving a fit to the median response sizes with an  $R^2 = 0.86$ . Deviations from this trend can possibly be explained by the enclosed sensing environment preventing sufficient mixing of electrolyte concentrations within the PDMS well, which could possibly be addressed by using a flow cell for sensing work. It was also seen that the signal size relative to baseline drift was highly consistent between channels. This is a promising result when it comes to ensuring consistent multiplexing, but it cannot be guaranteed that this behaviour carries over to sensing with biofunctionalised devices.

Graphene field-effect transistor devices were often found to possess a double-minima feature, which appears to be the result of a lack of doping from the metal contacts in the center of the device channels. These double Dirac points are unlikely to have an significant effect on the sensing behaviour of graphene devices. The graphene device characteristics were found to be consistent after 1 hour exposure to 1X PBS with minimal drift, with an on-off ratio of 5 and major Dirac point voltage of 0.3 V. There was some indications from the transfer characteristics that *p*-dopants were present on the graphene surface. Salt concentration sensing with graphene FETs is not shown in this thesis, but it is important to perform this experiment and use similar analysis techniques if there are any concerns about the sensitivity of a fabricated batch of graphene devices.

## A. Vapour System Hardware

Table A.1.: Major components used in construction of the vapour delivery system described in this thesis.

Description	Part No.	Manufacturer
Mass flow controller, 20 sccm full scale	GE50A013201SBV020	MKS Instruments
Mass flow controller, 200 sccm full scale	GE50A013202SBV020	MKS Instruments
Mass flow controller, 500 sccm full scale	FC-2901V	Tylan
Analogue flowmeter, 240 sccm max. flow	116261-30	Dwyer
Micro diaphragm pump	P200-B3C5V-35000	Xavitech
Analogue flow controller, for micro diaphragm pump	X3000450	Xavitech
10 mL Schott bottle	218010802	Duran
PTFE connection cap system	Z742273	Duran
Baseline VOC-TRAQ flow cell, red	043-951	Mocon
Humidity and temperature sensor	T9602	Telaire
Enclosure, for humidity and temperature sensor	MC001189	Multicomp Pro



## B. Python Code for Data Analysis

### B.1. Code Repository

The code used for general analysis of field-effect transistor devices in this thesis was written with Python 3.8.8. Contributors to the code used include Erica Cassie, Erica Happe, Marissa Dierkes and Leo Browning. The code is located on GitHub and the research group OneDrive, and is available on request.

### B.2. Atomic Force Microscope Histogram Analysis

The purpose of this code is to analyse atomic force microscope (AFM) images of carbon nanotube networks in .xyz format taken using an atomic force microscope and processed in Gwyddion (see [?@sec-afm-characterisation](#)). It was originally designed by Erica Happe in Matlab, and adapted by Marissa Dierkes and myself for use in Python. The code imports the .xyz data and sorts it into bins 0.15 nm in size for processing. To perform skew-normal distribution fits, both *scipy.optimize.curve\_fit* and *scipy.stats.skewnorm* modules are used in this code.

### B.3. Raman Spectroscopy Analysis

The purpose of this code is to analyse a series of Raman spectra taken at different points on a single film (see [?@sec-raman-characterisation](#)). Data is imported in a series of tab-delimited text files, with the low wavenumber spectrum ( $100\text{ cm}^{-1} - 650\text{ cm}^{-1}$ ) and high wavenumber spectrum ( $1300\text{ cm}^{-1} - 1650\text{ cm}^{-1}$ ) imported in separate datafiles for each scan location.

### B.4. Field-Effect Transistor Analysis

The purpose of this code is to analyse electrical measurements taken of field-effect transistor (FET) devices. Electrical measurements were either taken from the Keysight 4156C Semiconductor Parameter Analyser, National Instruments NI-PXIe or Keysight B1500A Semiconductor Device Analyser as discussed in [?@sec-electrical-characterisation](#);

### *B. Python Code for Data Analysis*

the code is able to analyse data in .csv format taken from all three measurement setups. The main Python file in the code base consists of three related but independent modules: the first analyses and plots sensing data from the FET devices, the second analyses and plots transfer characteristics from channels across a device, and the third compares individual channel characteristics before and after a modification or after each of several modifications. The code base also features a separate config file and style sheet which govern the behaviour of the main code. The code base was designed collaboratively by myself and Erica Cassie over GitHub using the Sourcetree Git GUI.

# Bibliography

- [1] H. Y. Zheng and N. O.V. Plank. “Facile fabrication of carbon nanotube network thin film transistors for device platforms”. In: *International Journal of Nanotechnology* 14.1-6 (2017), pp. 505–518. ISSN: 14757435. DOI: 10.1504/IJNT.2017.082473.
- [2] Thanihaichelvan Murugathas, Leo A. Browning, Marissa P. Dierkes, et al. “Data on liquid gated CNT network FETs on flexible substrates”. In: *Data in Brief* 21 (Dec. 2018), pp. 276–283. ISSN: 2352-3409. DOI: 10.1016/J.DIB.2018.09.093.
- [3] Thanihaichelvan Murugathas, Leo A. Browning, Marissa P. Dierkes, et al. “Metallic-semiconducting junctions create sensing hot-spots in carbon nanotube FET aptasensors near percolation”. In: *Biosensors and Bioelectronics* 130 (Apr. 2019), pp. 408–413. ISSN: 0956-5663. DOI: 10.1016/J.BIOS.2018.09.021.
- [4] Hong Phan T. Nguyen, Thanihaichelvan Murugathas, and Natalie O.V. Plank. “Comparison of Duplex and Quadruplex Folding Structure Adenosine Aptamers for Carbon Nanotube Field Effect Transistor Aptasensors”. In: *Nanomaterials (Basel, Switzerland)* 11.9 (Sept. 2021). ISSN: 2079-4991. DOI: 10.3390/NANO11092280. URL: <https://pubmed.ncbi.nlm.nih.gov/34578596/>.
- [5] Wim Wenseleers, Igor L. Vlasov, Etienne Goovaerts, et al. “Efficient Isolation and Solubilization of Pristine Single-Walled Nanotubes in Bile Salt Micelles”. In: *Advanced Functional Materials* 14.11 (Nov. 2004), pp. 1105–1112. ISSN: 1616-3028. DOI: 10.1002/ADFM.200400130. URL: <https://onlinelibrary.wiley.com/doi/full/10.1002/adfm.200400130%20https://onlinelibrary.wiley.com/doi/abs/10.1002/adfm.200400130%20https://onlinelibrary.wiley.com/doi/10.1002/adfm.200400130>.
- [6] Gildas Gavrel, Bruno Jousselme, Arianna Filoromo, et al. “Supramolecular Chemistry of Carbon Nanotubes”. In: (2013), pp. 95–126. DOI: 10.1007/128\_2013\_450.
- [7] Greg T. Hermanson. “Buckyballs, Fullerenes, and Carbon Nanotubes”. In: *Bioconjugate Techniques* (Jan. 2013), pp. 741–755. DOI: 10.1016/B978-0-12-382239-0.00016-9.
- [8] Maki Shimizu, Shunjiro Fujii, Takeshi Tanaka, et al. “Effects of surfactants on the electronic transport properties of thin-film transistors of single-wall carbon nanotubes”. In: *Journal of Physical Chemistry C* 117.22 (June 2013), pp. 11744–11749. ISSN: 19327455. DOI: 10.1021/JP3113254/SUPPL\_FILE/JP3113254\_SI\_001.PDF. URL: <https://pubs.acs.org/doi/full/10.1021/jp3113254>.

## Bibliography

- [9] Antonello Di Crescenzo, Valeria Ettorre, and Antonella Fontana. “Non-covalent and reversible functionalization of carbon nanotubes”. In: *Beilstein Journal of Nanotechnology* 5.1 (2014), p. 1675. ISSN: 21904286. DOI: 10.3762/BJNANO.5.178. URL: [/pmc/articles/PMC4222398/](https://pmc.ncbi.nlm.nih.gov/pmc/articles/PMC4222398/)?report=abstract%20https://www.ncbi.nlm.nih.gov/pmc/articles/PMC4222398/.
- [10] Melburne C. LeMieux, Mark Roberts, Soumendra Barman, et al. “Self-sorted, aligned nanotube networks for thin-film transistors”. In: *Science* 321.5885 (July 2008), pp. 101–104. ISSN: 00368075. DOI: 10.1126/SCIENCE.1156588. URL: <https://www.science.org>.
- [11] Chang Liu and Hui Ming Cheng. “Carbon nanotubes: controlled growth and application”. In: *Materials Today* 16.1-2 (Jan. 2013), pp. 19–28. ISSN: 1369-7021. DOI: 10.1016/J.MATTOD.2013.01.019.
- [12] Dusan Vobornik, Maohui Chen, Shan Zou, et al. “Measuring the Diameter of Single-Wall Carbon Nanotubes Using AFM”. In: *Nanomaterials* 13.3 (Feb. 2023), p. 477. ISSN: 20794991. DOI: 10.3390/NANO13030477/S1. URL: <https://www.mdpi.com/2079-4991/13/3/477>.
- [13] A. Azzalini and A. Capitanio. “Statistical applications of the multivariate skew normal distribution”. In: *Journal of the Royal Statistical Society Series B* 61.3 (1999), pp. 579–602. ISSN: 13697412. DOI: 10.1111/1467-9868.00194. arXiv: 0911.2093. URL: <https://ideas.repec.org/a/bla/jorss/v61y1999i3p579-602.html>%20https://ideas.repec.org//a/bla/jorss/v61y1999i3p579-602.html.
- [14] Matěj Velický, Adam J Cooper, Peter S Toth, et al. “Mechanical stability of substrate-bound graphene in contact with aqueous solutions”. In: *2D Materials* 2.2 (May 2015), p. 024011. ISSN: 2053-1583. DOI: 10.1088/2053-1583/2/2/024011. URL: [https://iopscience.iop.org/article/10.1088/2053-1583/2/2/024011%20https://iopscience.iop.org/article/10.1088/2053-1583/2/2/024011/meta](https://iopscience.iop.org/article/10.1088/2053-1583/2/2/024011).
- [15] Erin E. Christensen, Mitesh Amin, Trevor M. Tumiel, et al. “Localized Charge on Surfactant-Wrapped Single-Walled Carbon Nanotubes”. In: *Journal of Physical Chemistry Letters* 13.46 (Nov. 2022), pp. 10705–10712. ISSN: 19487185. DOI: 10.1021/ACS.JPCLETT.2C02650. URL: <https://pubs.acs.org/doi/full/10.1021/acs.jpclett.2c02650>.
- [16] R. L. Graham, B. D. Lubachevsky, K. J. Nurmela, et al. “Dense packings of congruent circles in a circle”. In: *Discrete Mathematics* 181.1-3 (Feb. 1998), pp. 139–154. ISSN: 0012-365X. DOI: 10.1016/S0012-365X(97)00050-2.
- [17] Eckard Specht. *The best known packings of equal circles in a circle*. URL: <http://hydra.nat.uni-magdeburg.de/packing/cci/cci.html> (visited on 2023-09-11).
- [18] Robert D. Deegan, Olgica Bakajin, Todd F. Dupont, et al. “Capillary flow as the cause of ring stains from dried liquid drops”. In: *Nature* 1997 389:6653 389.6653 (1997), pp. 827–829. ISSN: 1476-4687. DOI: 10.1038/39827. URL: <https://www.nature.com/articles/39827>.

- [19] R. T. van Gaalen, C. Diddens, H. M.A. Wijshoff, et al. “Marangoni circulation in evaporating droplets in the presence of soluble surfactants”. In: *Journal of Colloid and Interface Science* 584 (Feb. 2021), pp. 622–633. ISSN: 0021-9797. DOI: 10.1016/J.JCIS.2020.10.057.
- [20] Mindy D. Bishop, Gage Hills, Tathagata Srimani, et al. “Fabrication of carbon nanotube field-effect transistors in commercial silicon manufacturing facilities”. In: *Nature Electronics* 2020 3:8 3.8 (June 2020), pp. 492–501. ISSN: 2520-1131. DOI: 10.1038/s41928-020-0419-7. URL: <https://www.nature.com/articles/s41928-020-0419-7>.
- [21] Yulia V Marchenko and Marc G Genton. “A suite of commands for fitting the skew-normal and skew-t models”. In: *The Stata Journal* 10.4 (2010), pp. 507–539.
- [22] Alexander A. Kane, Alexandra C. Ford, April Nissen, et al. “Etching of surfactant from solution-processed, type-separated carbon nanotubes and impact on device behavior”. In: *ACS Nano* 8.3 (Mar. 2014), pp. 2477–2485. ISSN: 1936086X. DOI: 10.1021/NN406065T. URL: <https://pubs.acs.org/doi/full/10.1021/nn406065t>.
- [23] Millie S. Dresselhaus, G. Dresselhaus, R. Saito, et al. “Raman spectroscopy of carbon nanotubes”. In: *Physics Reports* 409.2 (Mar. 2005), pp. 47–99. ISSN: 0370-1573. DOI: 10.1016/J.PHYSREP.2004.10.006.
- [24] Benjamin King and Balaji Panchapakesan. “Vacuum filtration based formation of liquid crystal films of semiconducting carbon nanotubes and high performance transistor devices”. In: *Nanotechnology* 25.17 (Apr. 2014), p. 175201. ISSN: 0957-4484. DOI: 10.1088/0957-4484/25/17/175201. URL: <https://iopscience.iop.org/article/10.1088/0957-4484/25/17/175201%20https://iopscience.iop.org/article/10.1088/0957-4484/25/17/175201/meta>.
- [25] M. Świniarski, A. Dużyńska, A. P. Gertych, et al. “Determination of the electronic transport in type separated carbon nanotubes thin films doped with gold nanocrystals”. In: *Scientific Reports* 2021 11:1 11.1 (Aug. 2021), pp. 1–7. ISSN: 2045-2322. DOI: 10.1038/s41598-021-96307-6. URL: <https://www.nature.com/articles/s41598-021-96307-6>.
- [26] David C. Stone. “Application of median filtering to noisy data”. In: 73.10 (Oct. 2011), pp. 1573–1581. ISSN: 0008-4042. DOI: 10.1139/V95-195. URL: <https://cdnsciencepub.com/doi/10.1139/v95-195>.
- [27] Douglas R. Kauffman and Alexander Star. “Electronically monitoring biological interactions with carbon nanotube field-effect transistors”. In: *Chemical Society Reviews* 37.6 (May 2008), pp. 1197–1206. ISSN: 1460-4744. DOI: 10.1039/B709567H. URL: <https://pubs.rsc.org/en/content/articlehtml/2008/cs/b709567h%20https://pubs.rsc.org/en/content/articlelanding/2008/cs/b709567h>.

## Bibliography

- [28] Iddo Heller, Jaan Männik, Serge G. Lemay, et al. “Optimizing the signal-to-noise ratio for biosensing with carbon nanotube transistors”. In: *Nano Letters* 9.1 (Jan. 2009), pp. 377–382. ISSN: 15306984. DOI: 10.1021/NL8031636/SUPPL\_FILE/NL8031636\_SI\_001.PDF. URL: <https://pubs.acs.org/doi/full/10.1021/nl8031636>.
- [29] Woo Jong Yu, Un Jeong Kim, Bo Ram Kang, et al. “Adaptive Logic Circuits with Doping-Free Ambipolar Carbon Nanotube Transistors”. In: *NANO LETTERS* 9.4 (2009), pp. 1401–1405. DOI: 10.1021/nl803066v. URL: <https://pubs.acs.org/sharingguidelines>.
- [30] Vladimir Derenskyi, Widiantha Gomulya, Jorge Mario Salazar Rios, et al. “Carbon Nanotube Network Ambipolar Field-Effect Transistors with 108 On/Off Ratio”. In: *Advanced Materials* 26.34 (Sept. 2014), pp. 5969–5975. ISSN: 15214095. DOI: 10.1002/ADMA.201401395.
- [31] Faris M. Albarghouthi, Nicholas X. Williams, James L. Doherty, et al. “Passivation Strategies for Enhancing Solution-Gated Carbon Nanotube Field-Effect Transistor Biosensing Performance and Stability in Ionic Solutions”. In: *ACS Applied Nano Materials* 5.10 (Oct. 2022), pp. 15865–15874. ISSN: 25740970. DOI: 10.1021/ACSANM.2C04098. URL: <https://doi.org/10.1021/acsanm.2c04098>.
- [32] Eric Pop, Sumit Dutta, David Estrada, et al. “Avalanche, Joule breakdown and hysteresis in carbon nanotube transistors”. In: *IEEE International Reliability Physics Symposium Proceedings* (2009), pp. 405–408. ISSN: 15417026. DOI: 10.1109/IRPS.2009.5173287.
- [33] Nima Rouhi, Dheeraj Jain, Katayoun Zand, et al. “Fundamental limits on the mobility of nanotube-based semiconducting inks”. In: *Advanced Materials* 23.1 (Jan. 2011), pp. 94–99. ISSN: 09359648. DOI: 10.1002/ADMA.201003281.
- [34] Jana Zaumseil. “Single-walled carbon nanotube networks for flexible and printed electronics”. In: *Semiconductor Science and Technology* 30.7 (June 2015), p. 074001. ISSN: 0268-1242. DOI: 10.1088/0268-1242/30/7/074001. URL: <https://iopscience.iop.org/article/10.1088/0268-1242/30/7/074001%20https://iopscience.iop.org/article/10.1088/0268-1242/30/7/074001/meta>.
- [35] Xuan P A Gao, Gengfeng Zheng, and Charles M Lieber. “Subthreshold Regime has the Optimal Sensitivity for Nanowire FET Biosensors”. In: (2010). DOI: 10.1021/nl9034219. URL: <https://pubs.acs.org/sharingguidelines>.
- [36] Donghun Kang, Noejung Park, Ju Hye Ko, et al. “Oxygen-induced p-type doping of a long individual single-walled carbon nanotube”. In: *Nanotechnology* 16.8 (May 2005), p. 1048. ISSN: 0957-4484. DOI: 10.1088/0957-4484/16/8/008. URL: <https://iopscience.iop.org/article/10.1088/0957-4484/16/8/008%20https://iopscience.iop.org/article/10.1088/0957-4484/16/8/008/meta>.

- [37] Iddo Heller, Anne M. Janssens, Jaan Männik, et al. “Identifying the mechanism of biosensing with carbon nanotube transistors”. In: *Nano Letters* 8.2 (Feb. 2008), pp. 591–595. ISSN: 15306984. DOI: 10.1021/NL072996I. URL: <https://pubs.acs.org/doi/full/10.1021/nl072996i>.
- [38] Yoshiyuki Nonoguchi, Atsushi Tani, Tomoko Murayama, et al. “Surfactant-driven Amphoteric Doping of Carbon Nanotubes”. In: *Chemistry - An Asian Journal* 13.24 (Dec. 2018), pp. 3942–3946. ISSN: 1861471X. DOI: 10.1002/ASIA.201801490.
- [39] Chris J. Barnett, Cathren E. Gowenlock, Kathryn Welsby, et al. “Spatial and Contamination-Dependent Electrical Properties of Carbon Nanotubes”. In: *Nano letters* 18.2 (Feb. 2018), pp. 695–700. ISSN: 1530-6992. DOI: 10.1021 / ACS . NANOLETT.7B03390. URL: <https://pubmed.ncbi.nlm.nih.gov/29257695/>.
- [40] Joon Sung Lee, Sunmin Ryu, Kwonjae Yoo, et al. “Origin of gate hysteresis in carbon nanotube field-effect transistors”. In: *Journal of Physical Chemistry C* 111.34 (Aug. 2007), pp. 12504–12507. ISSN: 19327447. DOI: 10.1021/JP074692Q. URL: <https://pubs.acs.org/doi/full/10.1021/jp074692q>.
- [41] Sang Won Lee, Si Young Lee, Seong Chu Lim, et al. “Positive gate bias stress instability of carbon nanotube thin film transistors”. In: *Applied Physics Letters* 101.5 (July 2012). ISSN: 00036951. DOI: 10.1063/1.4740084/111432. URL: [/aip/apl/article/101/5/053504/111432/Positive-gate-bias-stress-instability-of-carbon](https://aip.org/apl/article/101/5/053504/111432/Positive-gate-bias-stress-instability-of-carbon).
- [42] Tae Jun Ha, Daisuke Kiriya, Kevin Chen, et al. “Highly stable hysteresis-free carbon nanotube thin-film transistors by fluorocarbon polymer encapsulation”. In: *ACS Applied Materials and Interfaces* 6.11 (June 2014), pp. 8441–8446. ISSN: 19448252. DOI: 10.1021/AM5013326. URL: <https://pubs.acs.org/doi/full/10.1021/am5013326>.
- [43] Woong Kim, Ali Javey, Ophir Vermesh, et al. “Hysteresis Caused by Water Molecules in Carbon Nanotube Field-Effect Transistors”. In: *NANO LETTERS* 3.2 (2003), pp. 193–198. DOI: 10.1021/nl0259232.
- [44] Aaron D. Franklin, George S. Tulevski, Shu Jen Han, et al. “Variability in carbon nanotube transistors: Improving device-to-device consistency”. In: *ACS Nano* 6.2 (Feb. 2012), pp. 1109–1115. ISSN: 19360851. DOI: 10.1021/NN203516Z. URL: <https://pubs.acs.org/doi/full/10.1021/nn203516z>.
- [45] Helene Conseil, Morten S. Jellesen, and Rajan Ambat. “Experimental study of water absorption of electronic components and internal local temperature and humidity into electronic enclosure”. In: *Proceedings of the 16th Electronics Packaging Technology Conference, EPTC 2014* (Jan. 2014), pp. 355–359. DOI: 10.1109 / EPTC.2014.7028356.
- [46] I. Heller, S. Chattoor, J. Männik, et al. “Comparing the weak and strong gate-coupling regimes for nanotube and graphene transistors”. In: *physica status solidi (RRL) – Rapid Research Letters* 3.6 (Sept. 2009), pp. 190–192. ISSN: 1862-6270. DOI: 10.1002/PSSR.200903157. URL: <https://onlinelibrary.wiley.com/doi/full/>

## Bibliography

- 10.1002/pssr.200903157%20https://onlinelibrary.wiley.com/doi/abs/10.1002/pssr.200903157%20https://onlinelibrary.wiley.com/doi/10.1002/pssr.200903157.
- [47] Iddo Heller, Sohail Chatoor, Jaan Männik, et al. “Influence of electrolyte composition on liquid-gated carbon nanotube and graphene transistors”. In: *Journal of the American Chemical Society* 132.48 (Dec. 2010), pp. 17149–17156. ISSN: 00027863. DOI: 10.1021/JA104850N/SUPPL\_FILE/JA104850N\_SI\_001.PDF. URL: <https://pubs.acs.org/doi/full/10.1021/ja104850n>.
- [48] Fengnian Xia, Damon B. Farmer, Yu Ming Lin, et al. “Graphene field-effect transistors with high on/off current ratio and large transport band gap at room temperature”. In: *Nano Letters* 10.2 (Feb. 2010), pp. 715–718. ISSN: 15306984. DOI: 10.1021/NL9039636/ASSET/IMAGES/LARGE/NL-2009-039636\_0003.JPG. URL: <https://pubs.acs.org/doi/full/10.1021/nl9039636>.
- [49] Dmitry Kireev, Max Brambach, Silke Seyock, et al. “Graphene transistors for interfacing with cells: towards a deeper understanding of liquid gating and sensitivity”. In: *Scientific Reports* 2017 7:1 7.1 (July 2017), pp. 1–12. ISSN: 2045-2322. DOI: 10.1038/s41598-017-06906-5. URL: <https://www.nature.com/articles/s41598-017-06906-5>.
- [50] Antonio Di Bartolomeo, Filippo Giubileo, Salvatore Santandrea, et al. “Charge transfer and partial pinning at the contacts as the origin of a double dip in the transfer characteristics of graphene-based field-effect transistors”. In: *Nanotechnology* 22.27 (May 2011), p. 275702. ISSN: 0957-4484. DOI: 10.1088/0957-4484/22/27/275702. URL: [https://iopscience.iop.org/article/10.1088/0957-4484/22/27/275702/meta](https://iopscience.iop.org/article/10.1088/0957-4484/22/27/275702%20https://iopscience.iop.org/article/10.1088/0957-4484/22/27/275702/meta).
- [51] Zengguang Cheng, Qiaoyu Zhou, Chenxuan Wang, et al. “Toward intrinsic graphene surfaces: A systematic study on thermal annealing and wet-chemical treatment of SiO<sub>2</sub>-supported graphene devices”. In: *Nano Letters* 11.2 (Feb. 2011), pp. 767–771. ISSN: 15306984. DOI: 10.1021/NL103977D/SUPPL\_FILE/NL103977D\_SI\_001.PDF. URL: <https://pubs.acs.org/doi/full/10.1021/nl103977d>.
- [52] Dong Wook Shin, Hyun Myoung Lee, Seong Man Yu, et al. “A facile route to recover intrinsic graphene over large scale”. In: *ACS Nano* 6.9 (Sept. 2012), pp. 7781–7788. ISSN: 19360851. DOI: 10.1021/NN3017603/SUPPL\_FILE/NN3017603\_SI\_001.PDF. URL: <https://pubs.acs.org/doi/full/10.1021/nn3017603>.
- [53] Tingting Feng, Dan Xie, Jianlong Xu, et al. “Back-gate graphene field-effect transistors with double conductance minima”. In: *Carbon* 79.1 (Nov. 2014), pp. 363–368. ISSN: 0008-6223. DOI: 10.1016/J.CARBON.2014.07.078.
- [54] Song ang Peng, Zhi Jin, Dayong Zhang, et al. “How Do Contact and Channel Contribute to the Dirac Points in Graphene Field-Effect Transistors?” In: *Advanced Electronic Materials* 4.8 (Aug. 2018), p. 1800158. ISSN: 2199-160X. DOI: 10.1002/AELM.201800158. URL: <https://onlinelibrary.wiley.com/doi/full/10.1002/AELM.201800158>.

- aelm. 201800158%20https://onlinelibrary.wiley.com/doi/abs/10.1002/aelm.201800158%20https://onlinelibrary.wiley.com/doi/10.1002/aelm.201800158.
- [55] Y. Bargaoui, M. Troudi, P. Bondavalli, et al. “Gate bias stress effect in single-walled carbon nanotubes field-effect-transistors”. In: *Diamond and Related Materials* 84 (Apr. 2018), pp. 62–65. ISSN: 0925-9635. DOI: 10.1016/J.DIAMOND.2018.03.011.
- [56] Steven G. Noyce, James L. Doherty, Zhihui Cheng, et al. “Electronic Stability of Carbon Nanotube Transistors under Long-Term Bias Stress”. In: *Nano Letters* 19.3 (Mar. 2019), pp. 1460–1466. ISSN: 15306992. DOI: 10.1021/ACS.NANOLETT.8B03986. URL: <https://pubs.acs.org/doi/full/10.1021/acs.nanolett.8b03986>.
- [57] H. Lin and S. Tiwari. “Localized charge trapping due to adsorption in nanotube field-effect transistor and its field-mediated transport”. In: *Applied Physics Letters* 89.7 (Aug. 2006), p. 73507. ISSN: 00036951. DOI: 10.1063/1.2337104. URL: [/aip/apl/article/89/7/073507/332595/Localized-charge-trapping-due-to-adsorption-in](https://aip.org/apl/article/89/7/073507/332595/Localized-charge-trapping-due-to-adsorption-in).
- [58] Sandeep Agnihotri, Mark J. Rood, and Massoud Rostam-Abadi. “Adsorption equilibrium of organic vapors on single-walled carbon nanotubes”. In: *Carbon* 43.11 (Sept. 2005), pp. 2379–2388. ISSN: 0008-6223. DOI: 10.1016/J.CARBON.2005.04.020.
- [59] Chang Young Lee and Michael S. Strano. “Understanding the dynamics of signal transduction for adsorption of gases and vapors on carbon nanotube sensors”. In: *Langmuir* 21.11 (May 2005), pp. 5192–5196. ISSN: 07437463. DOI: 10.1021/LA046867I/ASSET/IMAGES/LARGE/LA046867IF00003.JPG. URL: <https://pubs.acs.org/doi/full/10.1021/la046867i>.
- [60] Nimibofa Ayawei, Augustus Newton Ebelegi, and Donbebe Wankasi. “Modelling and Interpretation of Adsorption Isotherms”. In: *Journal of Chemistry* 2017 (2017). ISSN: 20909071. DOI: 10.1155/2017/3039817.
- [61] Mohammad Mehdi Sabzehmeidani, Sahar Mahnaee, Mehrorang Ghaedi, et al. “Carbon based materials: a review of adsorbents for inorganic and organic compounds”. In: *Materials Advances* 2.2 (Feb. 2021), pp. 598–627. ISSN: 26335409. DOI: 10.1039/DOMA00087F. URL: <https://pubs.rsc.org/en/content/articlehtml/2021/ma/d0ma00087f%20https://pubs.rsc.org/en/content/articlelanding/2021/ma/d0ma00087f>.
- [62] “piD-TECH® eVx User Manual 143-175 Rev 1.0”. URL: <https://www.ametekmocon.com/products/oemphotoionization/pidtechevxphotoionizationdetector>.
- [63] *Technical Application Articles - Ion Science UK*. URL: <https://ionscience.com/en/gas-and-leak-detectors/customer-support/support-documents/technical-application-articles/> (visited on 2024-02-27).